Design of a magnetic shape memory actuator

Thesis

TO ACHIEVE THE ACADEMIC DEGREE OF

Master in Mechatronics

BY

Héctor Manuel Zamora García de León

Santiago de Querétaro, Querétaro, February 2017

Declaration of Authorship

I hereby declare that the thesis submitted is my own unaided work. All direct or indirect sources used are acknowledged as references.

I am aware that the thesis in digital form can be examined for the use of unauthorized aid and in order to determine whether the thesis as a whole or parts incorporated in it may be deemed as plagiarism. For the comparison of my work with existing sources I agree that it shall be entered in a database where it shall also remain after examination, to enable comparison with future theses submitted. Further rights of reproduction and usage, however, are not granted here.

This work was not previously presented to another examination board and has not been published.

Queretaro, February 2017

Acknowledgements

I'd like to thank first of all to my supervisor Prof. Dr. rer. nat. Klaus Peter Kämper for all the support given through the development of this thesis. With his knowledge and guidance this project came to a good end.

Second I'd like to thank to Dipl. Ing. Gabriele Quester and my colleagues on the Microtechnology Laboratory Amélie and Harshvardhan ; their advices and support were crucial to get the expected results on the experiments designed.

Third I'd like to thanks all the personal on the FH-Aachen which contributed to the fabrication of the necessary parts; the people of Additive Manufacturing laboratory and the people in the Mechanical workshop.

Also I'd like to thank CONACYT and CIDESI for giving me the opportunity to study in this master degree program. Finally I'd like to thank my parents, they gave me the necessary support during difficult time. Without their support, things would not have came as expected.

Abstract

Smart materials are one of the technologies that are being used to develop different types of actuators. They have characteristics that allow them to be used directly as acting materials or sensing materials; they do not need an extra mechanism to adequate themselves to an actuator or sensor. The following work will focus on how a Magnetic Shape Memory Alloy can be included into a design of a linear actuator.

Magnetic Shape Memory Alloys are smart materials which change their shape in presence of an external magnetic field. They rely on the magnetic anisotropy of their basic lattice configuration.

Mathematical models, data acquisition programs, and finite element simulations were made to characterise the actuator described on this thesis.

Contents

List of Figures

List of Tables

Chapter 1

Introduction

With the development of new materials, it is inevitable to think on new kind of actuators based on what are called smart materials. The actuator selection for automating a process plant depends on the nature of the surroundings of the place where the actuator is being installed. Most of the times, the rational answers to which actuator must be used on the facilities are pneumatic, electromagnetic, hydraulic, thermal forces or actuators based on the piezoelectric effect.

One kind of smart material, is the so called Shape Memory Material. The present work, will focus on the Magnetic Shape Memory (MSM) Materials first described by [1]. These materials have large magnetic-induced strain with a short response time. Several studies are being carried out, to develop thin film deposition techniques for these materials [2, 3]. Also some practical applications such as the measurement and control of the vibration of a rotor, development of fluid pumps, and similar are being developed.

The current work is intended to develop a test bench of a magnetic shape memory alloy actuator on a macro scale. The design of the parts and characterisation of the actuator are discussed along with the results.

The layout of this thesis is as follows: Chapter 2 describes the foundations to understand the phenomena that drive the way these materials work. Also, there is a small explanation on how an MSM alloy can be used in practice, and finally to close the chapter, some of the basic configurations on how an actuator can be assembled are presented. Chapters 3 and 4 describe the design steps with different mathematical models, specifications and simulation results regarding the design of the actuator. Finally in Chapter

5 the results of the experiment are presented. A small explanation on how the data was acquired and processed is discussed.

Chapter 2

Shape Memory Effect

Smart materials are materials which have characteristics that can be controlled by certain external stimuli. The stimuli can include among others, change of temperature, moisture, change of pH of the surrounding medium, change of electric or magnetic field or applied mechanical stress.

Shape memory materials (SMMs) are featured by the ability to recover their original shape from a significant and seemingly plastic deformation when a particular stimulus is applied [4]. Among this class of materials, one can find what are called Shape Memory Alloys and Shape Memory Polymers.

Magnetic Shape Memory Alloys (MSMA) are materials that show a Shape Memory Effect. This effect is triggered by an external magnetic field.

2.1 Magnetic Shape Memory Effect

The Magnetic Shape Memory Effect presents on different alloys. This effect gives the material the ability to "remember" a state after this state has been modified. These states are achieved by applying a magnetic field on the material, and in some cases applying a temperature change and mechanical forces. The mechanism of this behaviour lies in the inner crystalline structure of the materials and the way the lattices are generated on the material.

The most common MSM material is a monocrystalline Ni-Mn-Ga Heusler alloy (face cubic crystal structure). Although there are other alloys [5, 6] that can be considered as MSMA they are not that common in the literature.

To obtain the MSM materials, the samples are cooled forming martensite variants. These variants have the same crystallographic structure but different orientation. A twin in a crystalline solid occurs between two adjacent regions of the same crystal lattice, where one of the regions is related to the other by a simple shear [7].

The mechanical stress needed to move the twin boundaries is called twinning stress. If no twin variants are present on the material, it is said that the material is in a single variant state. In MSM materials the twinning occurs on different length scales in a hierarchical manner [8].

Some of the characteristics measured by [9] of the Ni-Mn-Ga alloy are presented on Table 2.1.

Table 2.1: Single-crystal Ni-Mn-Ga Characteristics

Parameter	Value
Lattice parameters	$a = 0.594; b = 0.594; c = 0.559\ nm$
Cell volume	$0.197\ nm^3$
$\epsilon_0 = (1 - c/a)$	5.89%
Start twin stress	$1.0\ MPa$
Finish twin stress	$2.1\ MPa$
MSM strain	5.8%

2.1.1 Magnetically Induced Martensite (MIM) and Magnetically Induced Reorientation (MIR)

The magnetic-field induced strain in the magnetic shape memory alloys can occur in two ways: Magnetically Induced Martensite (MIM) and Magnetically Induced Reorientation (MIR). In the martensitic phase the MSM crystal is composed of different areas called twin variants, having different orientations of the easy axis of magnetization [10]. In Figure 2.1

the different orientations of the twin variants are shown. This twin structures have to be highly mobile in order to achieve a reorientation of the microstructure of the material.

Magnetically Induced Martensite happens when the material exhibits an austenite(cubic) phase originally. In martensite phase, two different axis a and c (with the c axis shorter than the a axis) are located along the hard and easy axis of magnetization of the lattice respectively. When a magnetic field is applied, the microstructures align themselves to the direction of the field inducing a martensite transformation. This alignment changes the overall shape of the MSM element by the ratio a/c. The material returns to the original phase when the magnetic field is removed. Figure 2.2 *b)* represents the MIM transformation.

Magnetically Induced Reorientation happens when the material has a martensitic phase originally. Since the material is ferromagnetic, individual magnetic dipoles are located in every elementary cell. These dipoles are located parallel to the c axis. When a magnetic field is applied to the material, the dipoles arrange themselves along the direction of the magnetic field, inducing a transformation into another twin variant. This change of variant results in the change of length of the material. In Figure 2.2 *a)* one can see the mechanism of how the MIR works. It can be seen that by reversing the direction of the magnetic field, the lattices do not orient back to the original form. Returning to the original martensite variant can be done by applying a mechanical stress or by applying a magnetic field rotated by 90°.

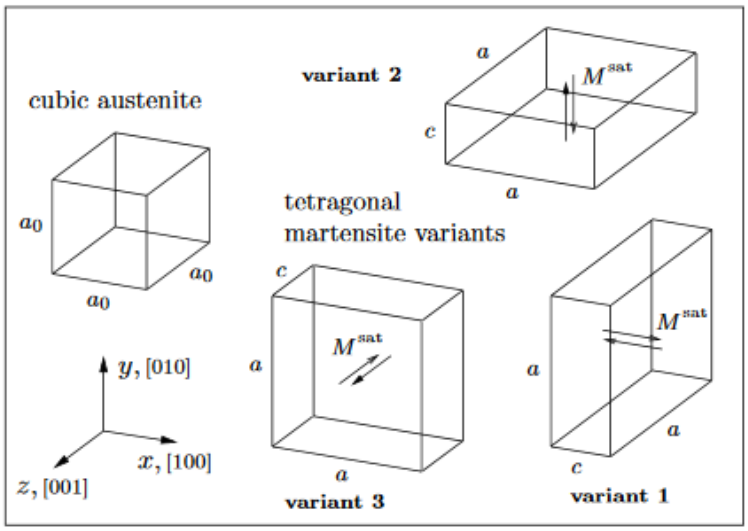

Figure 2.1: Representation of austenite and martensite phases. Martensites variants are also shown [11]

As the material used (5M-martensite type-$Ni_{50}Mn_{28}Ga_{22}$) is tetragonal in structure, the change in length of the material corresponds to the ratio a/c. This difference in magnitude (length of the a and c axis of the crystalline structure), which at micro levels is just hundredths of a nanometres, is responsible for the large deformation achievable on the macro level, as this minimum relative change of length will be multiplied several times depending on the length of the material.

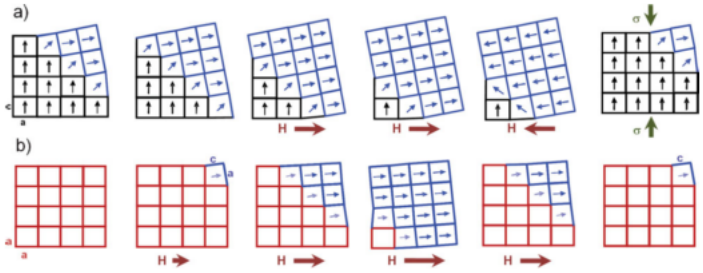

Figure 2.2: Magnetically Induced Martensite and Magnetically Induced Reorientation [12]

2.2 Modes of operation

The MSM alloys can work under one of the following operation methods: the first method consists of elongating and compressing the material by means of a mechanical force. This elongation force must be higher than the twinning stress. This mode of operation is particularly used in the development of vibration sensors. One must be careful while using this mode of operation, since the tensile strength of the material is quite low.

The second method of operation consists in applying a magnetic field normal to the easy axis of magnetization to elongate the MSMA. To return the material to its original shape, an external force is applied to compress the material. This has the drawback that the material has to overcome some pre-stress (if applied) which may reduce the stroke of the material.

The third mode acts as the opposite of the previous: the elongation is done by applying compressive force acting normal to the elongating side. The return to the previous state is by applying a field along the elongating direction.

The fourth mode has a similar actuating way; instead of applying a compressive force on a face normal to the elongating axis, the force responsible to elongate the material is

a tensile one. The return is made by a magnetic field parallel to the elongation force. This method is not recommended due to the fragility of the material and can break the material while elongating.

The fifth mode is the most desirable but also the most complex to achieve: both states, elongated and compressed, are achieved by the use of magnetic fields. These magnetic fields have to be orthogonal to each other and aligned with the axis of magnetization.

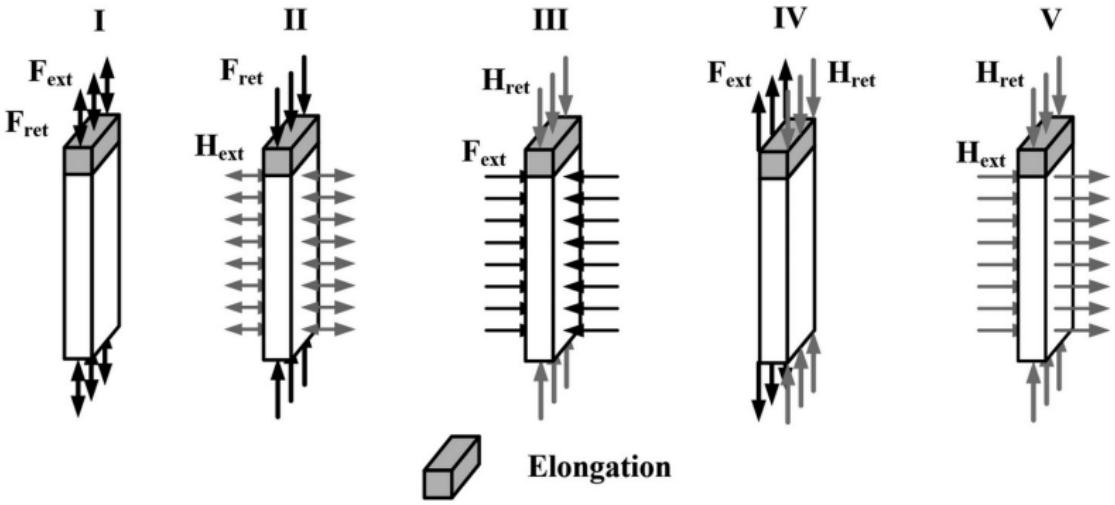

Figure 2.3: Operation modes of MSM alloys [13]

2.3 Types of actuators

MSM based actuators have been developed using the different modes of operation. Almost all of them fall into three categories: the return by a spring actuator, the push-push actuator and the push-pull actuator. In addition, there are actuators based on the change of cross-sectional area of the actuating element [14, 15, 16], but this work will focus on the first three.

The return spring actuator is based on the second mode of operation. The compressive force is applied by a spring and the magnetic field is generated by a magnetic circuit surrounding the actuator.

The push-push actuator is an arrangement of two MSM elements, in a collinear way. The actuator is based on the same mode of operation as before. Two MSM crystals are

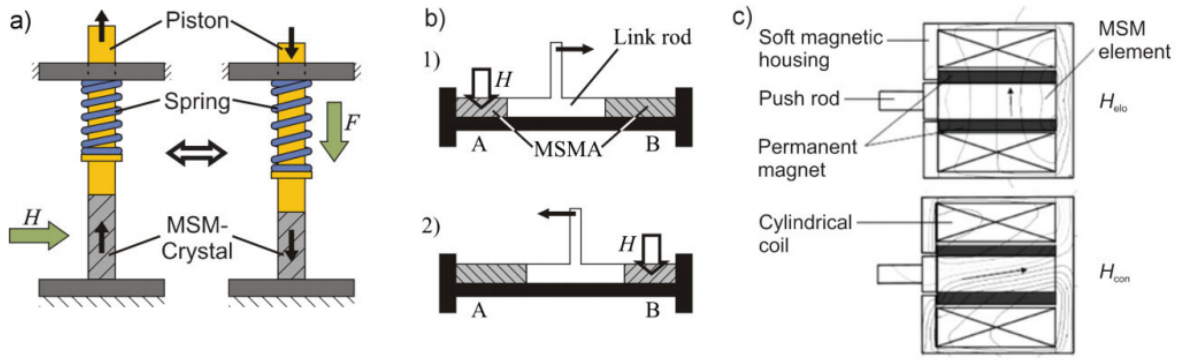

Figure 2.4: Kind of actuators. Basic sketches from [17].

activated by two coils, one per element. The movement is accomplished by activating either one of the coils, the force generated from one crystal contracts the other. This method has the advantage that the position of the final effector can be maintained with no current supplied to the coils.

The push-pull actuator works based on the fifth mode of operation: one permanent magnet is embedded into the actuator providing the necessary magnetic field to activate the elongated state, while the magnetic field provided by a coil counteracts the effects of the magnet, thus returning the material to the contracted shape.

In Figure 2.4 the basic sketches of the most common kind of actuators are shown. The spring actuator is shown in *a)*, the push-push actuator is shown in *b)* and the push-pull actuator is shown in *c)*.

Chapter 3

Design of magnetic circuit

According to [17] the first steps that should be taken into consideration to design a Magnetic Shape Memory Alloy-based actuator is to define the electromagnetic circuit responsible for generating the magnetic field for the system.

3.1 Calculation of the magnetic circuit

For the calculation of the defining values for the electromagnetic circuit, a simple magnetic-electric analogy is taken into consideration. An electrical circuit can be simplified by means of the transformation of voltage and current sources.

Hopkinson's Law relates the magnetomotive force (MMF), magnetic flux and reluctance the same way Ohm's Law relates electromotive force (EMF), current and resistance. The magnetomotive force $\mathcal{F}$ is the phenomena that takes place in certain substances or solids that gives rise to magnetic fields.

The magnetomotive force can be expressed as one of the three following formulae. Equation 3.1 is used to calculate the amount of flux density a solenoid can deliver. Equation 3.2 is Hopkinson's law (described before). Equation 3.3 is the simplified version of Ampere's circuital law $\oint_C H \cdot dl$.

$$\mathcal{F} = Ni \tag{3.1}$$

$$\mathcal{F} = \Phi\mathcal{R} \tag{3.2}$$

$$\mathcal{F} = Hl \tag{3.3}$$

where:
$\mathcal{F}$ is the magnetomotive force $[A \cdot turn]$
N is number of turns in a coil or a toroid $[turns]$
i is the current passing through the windings of the coil $[A]$
Φ is the magnetic flux flowing through the magnetic circuit $[Wb]$
$\mathcal{R}$ is the reluctance of the material $[H^{-1}]$
H is the magnetizing force in the circuit $[A/m]$
l is the mean length of the coil or toroid affected by the magnetizing force $[m]$

The previous equations represent the main equations that will be used to create a mathematical model. The following section is focused on the calculation of the term magnetic length in different models. This *magnetic length* represents the average distance a magnetic field line must travel in a medium (magnetic core, air or MSM element) in order to complete a loop. This magnetic length is important to the model since it will define the overall dimensions of the magnetic core. If the magnetic core is too large, the magnetic field generated will not be sufficient.

3.1.1 Core models

For the development of the present actuator, three different arrangements for the laminated core were taken into consideration, to verify that the geometry selected will provide the required flux density on the MSM element. The selected shapes are the most commonly used in practice due to their effectiveness and simplicity. In the Figure 3.1, sketches are presented to visualize the contemplated models. The location of the coils is not shown in the sketches.

A laminated core is used to compensate for Eddy currents. When a magnetic field passes through a conductor, circular currents are induced in planes normal to the direction of the magnetic field (according to Faraday's law of induction). These currents are generated by a fluctuating magnetic field such as in an AC magnetic field. According to Lenz's Law, these loops will generate a magnetic field opposing the one that generated them. The opposing magnetic fields cause losses on the material which are dissipated as heat.

In order to reduce the core losses caused by Eddy currents, a laminated core is used. The laminations, electrically isolated by varnish or lacquer, modify the path on which these current loops travel. The resulting Eddy currents on each lamination, make the electrons accumulate on the boundaries of the lamination; in this way these electrons prevent more electrical charges to accumulate on the lamination, thus suppressing the Eddy current effects.

In the upcoming designs, two coils are considered throughout as part of the three models.

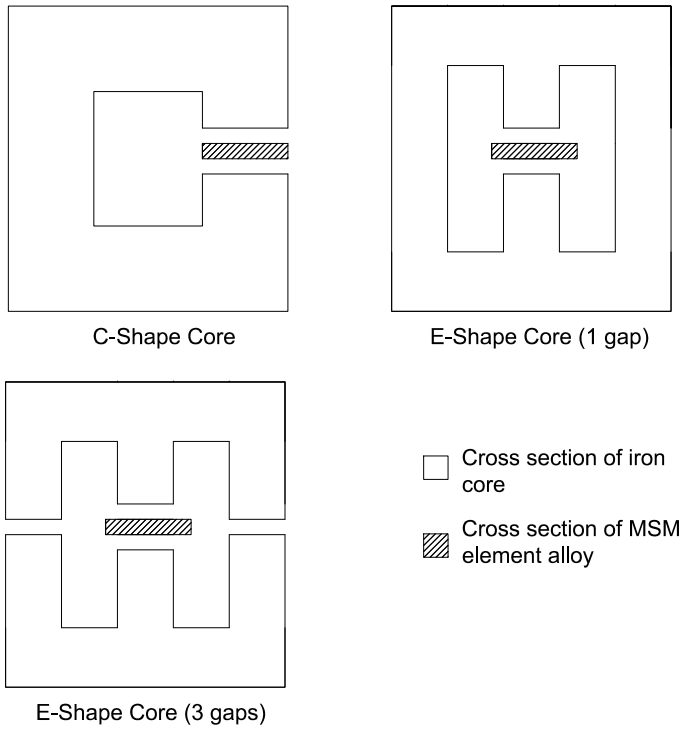

Figure 3.1: Selected cores designs for analysis.

The following formulas describe the behaviour of the model.

$$B = \mu H \tag{3.4}$$

$$\Phi_B = \iint_S B \, dS \tag{3.5}$$

$$H = \frac{l}{\mu S} \tag{3.6}$$

where:
B is the flux density $[T]$
μ is the permeability of the material $[H/m]$
dS represents an infinitesimal cross sectional area of the medium. When modelling different materials with different cross sections, one must consider the corresponding cross section $[m^2]$
l is the length of the active medium. For example in a solenoid it refers to the length of the coil $[m]$

To make this analysis and the relationship between magnetic and electrical components, some assumptions and idealizations are made:

- There are no ohmic losses in the coils. If considered, one must modify and add an element representing a loss in the magnetic circuit.
- The B-H curve is linear (only for hand calculations) and $\mu_m >> \mu_0$
- The mean length of the magnetic circuit is much greater than length of the gap and also the cross sectional area of the gap is much greater than the gap distance squared $(l_m >> l_g, A_g >> l_g^2)$
- Fringe effects are not taken into consideration

C-Shape Core

This configuration is the simplest in terms of modelling since it only has one gap and one way for the field lines to flow. Usually the gap in this kind of cores, is introduced to reduce the effect of magnetic saturation and to have a larger linear region on the B-H curve of the materials.

In the Figure 3.2 the coils are shown connected in series so that the vectors of magnetic flux lines are added and not subtracted among each other. The subindexes g and c stand for gap and core. The reluctance of the core is modelled as one length regardless of the position of the coils. The equations described in the section 3.1 as well the ones from section 3.1.1 and Kirchhoff's Law's are used to simplify the model. The goal of this simplification is to obtain one reasonable and achievable magnetic length.

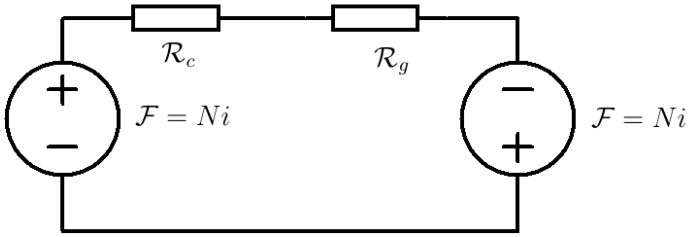

Figure 3.2: Analogous electrical model of the C-shape core.

Using Kircchoff's Voltage Law (KVL), the equation describing the circuit in Figure 3.2 is:

$$\sum_k \mathcal{R}_k \Phi = Ni \tag{3.7}$$

Therefore the expansion of the sum is the following:

$$\mathcal{R}_c\Phi + \mathcal{R}_g\Phi = 2Ni \Rightarrow \Phi(\mathcal{R}_c + \mathcal{R}_g) = 2Ni \tag{3.8}$$

Since it is assumed that the B-H curve is linear and also that all of the flux is transmitted (no fringe effects, therefore the cross sectional area of the gap and the core is the same) one can deduced the following:

$$2Ni = BA\left(\frac{l_c}{\mu_r\mu_0 A_c} + \frac{l_g}{\mu_0 A_g}\right) \tag{3.9}$$
$$\frac{2Ni}{B} = \frac{l_c}{\mu_r\mu_0} + \frac{l_g}{\mu_0}$$

$$\begin{aligned} l_c &= \left(\frac{2Ni}{B}\frac{l_g}{\mu_0}\right)\mu_r\mu_0 \\ &= \frac{2Ni\mu_r\mu_0}{B} - l_g\mu_r \end{aligned} \tag{3.10}$$

E-Shape Core (3 gaps)

This configuration contains 3 gaps augmenting the equivalent reluctance of the circuit. Including extra gaps to the core will result in a higher loss, nevertheless the model is

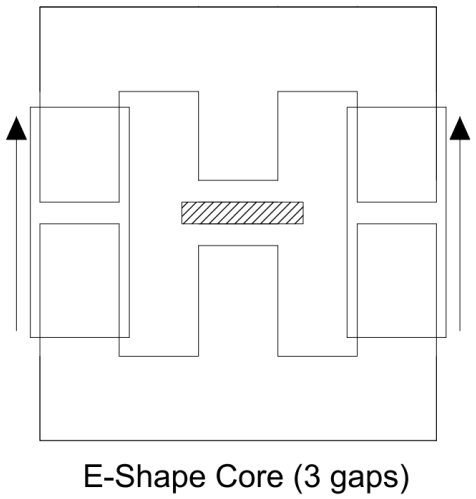

Figure 3.3: Sketch of the layout of the magnetic core using an E-shaped lamination.

analysed as a comparison between different designs. The current sources are placed on both legs of the core as shown in the Figure 3.3

The corresponding electric circuit is shown on Figure 3.4

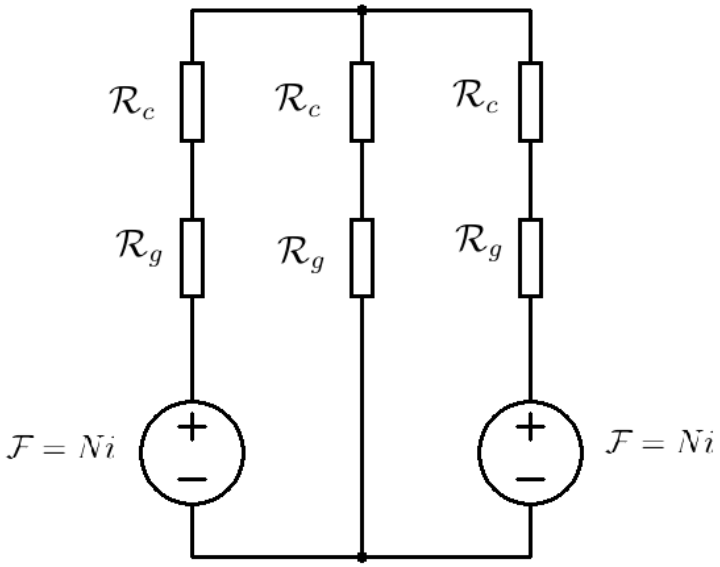

Figure 3.4: Electrical circuit showing the layout of the reluctances and coils for E-shape core (3 gaps)

In this case the sources are not connected in series but in parallel, which allows them to be simplified treating them as if they were current sources.

After reducing the terms (reluctances and current/voltage sources) one can find that

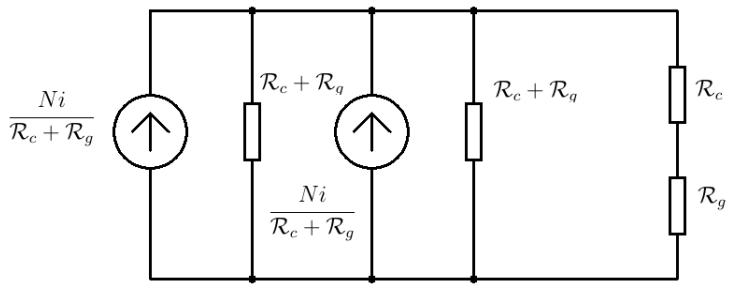

Figure 3.5: Transformation of sources of the circuit for E-shape core (3 gaps)

the equations are similar:

$$Ni = \Phi\left(\frac{3}{2}\mathcal{R}_c + \frac{3}{2}\mathcal{R}_g\right) = \frac{3}{2}BA\left(\frac{l_c}{\mu_r\mu_0 A_c} + \frac{l_g}{\mu_0 A_g}\right) \tag{3.11}$$

$$Ni = \frac{3}{2}B\left(\frac{l_c}{\mu_r\mu_0} + \frac{l_g}{\mu_0}\right) \tag{3.12}$$

$$\begin{aligned} l_c^{'} &= \left(\frac{2Ni}{3B} - \frac{l_g}{\mu_0}\right)\mu_0\mu_r \\ &= \frac{2Ni}{3B}\mu_0\mu_r - l_g\mu_r \end{aligned} \tag{3.13}$$

E-Shape Core (1 gap)

This configuration contains just one gap in order to place the MSM element. The same method to reduce the terms is applied as the previous circuit.

The corresponding electric circuit and transformed circuit are shown on Figures 3.6 and 3.7.

The equations describing the model are:

$$Ni = \Phi\left(\frac{3}{2}\mathcal{R}_c + \mathcal{R}_g\right) = \frac{3}{2}BA\left(\frac{l_c}{\mu_r\mu_0 A_c} + \frac{l_g}{\mu_0 A_g}\right) \tag{3.14}$$

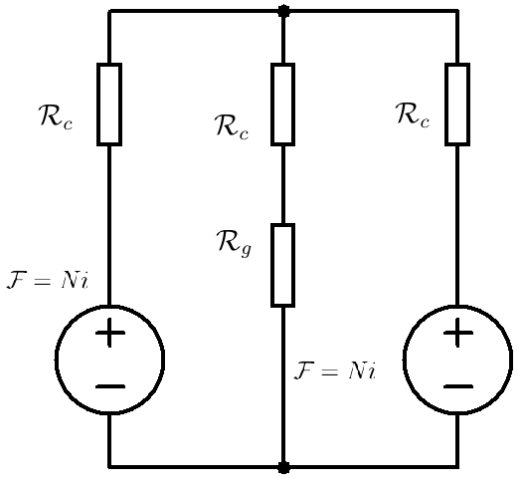

Figure 3.6: Electrical circuit showing the layout of the reluctances and coils for the third layout

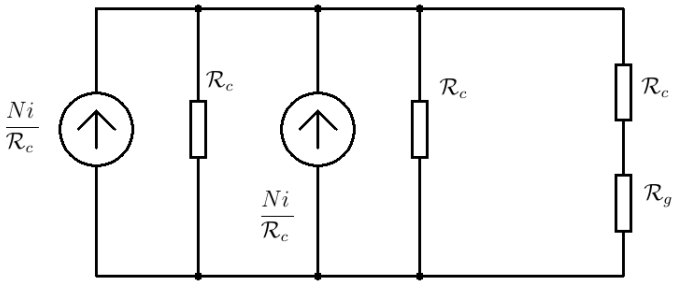

Figure 3.7: Transformation of sources for the analysis of the third layout (E-shape core with one gap)

$$Ni = \frac{3}{2}B\left(\frac{l_c}{\mu_r\mu_0} + \frac{l_g}{\mu_0}\right) \tag{3.15}$$

$$l_c' = \left(\frac{Ni}{B} - \frac{l_g}{\mu_0}\frac{2}{3}\right)\mu_0\mu_r = \frac{2Ni}{3B}\mu_0\mu_r - \frac{2}{3}l_g\mu_r \tag{3.16}$$

Having all the model's equations, one is able to see the effect of the different configurations considered in this study. The best design with minimum magnetic length is the C-shape core (Equation 3.10) , since the first term of the equation is not multiplied by a third. On the other hand the E-shape models, have a factor of a third where the MMF is located but the difference is on the term of the length of the gap. While in equation 3.13 the length of the gap is not multiplied by any factor, in 3.16 the length is reduced by a factor of 2/3 which is beneficial to the design. This factor together with the use of a

soft magnetic material will give the core the capacity to operate in the linear region of the B-H curve without reaching magnetic saturation. Continuing with the design features, the E-shape core is selected since it can be easily adapted to a symmetric mechanical structure.

According to studies [18, 19], a magnetic flux density starting from 0.2 T passing through the MSM material will overcome the twinning stress of the crystal with no external stress applied. This results in deformation of the MSM material. The flux density required to attain maximum strain is stress-dependent, but on these studies the maximum magnitude of this flux density is 1.5 T. For design purposes the operating magnetic field is considered to be 1 T.

The operating temperature of the MSM element should be below $40 - 60°C$. If the element reaches this temperature, the crystalline structure starts to change to an austenite phase (this phase is often related to Curie's temperature, which is the temperature at which a ferromagnetic material loses its permanent magnetic properties-) reducing the possible magnetic shape memory effect [20]. In order for the actuator to operate at regular temperatures that do not affect the crystalline structure of the MSM element, a low winding current is preferable. The amount of current a wire can carry without overheating, is determined by Joule heating. The rule of thumb for bundled wires without external cooling gives the maximum current carrying capacity. The maximum current is dependant on the diameter of the wire.

In this case, the design takes the maximum current using this rule of thumb, being the operating current of the actuator 2 A. The diameter of the wire was kept relatively small $0.8128 - 1.024mm$ (AWG20-AWG18) to get more turns of conductor per unit volume.

The gap between the tapered legs of the core (where the MSM element is located) was designed to be as small as possible to decrease the reluctance of the magnetic core. Since the MSM element must be free from external friction forces, a suitable gap distance was assumed. The gap was considered to be $0.5 - 1$ mm for the calculations.

Having all of the previous parameters and considerations, a spreadsheet using the formulae in this section was created to determine the optimum values for number of turns, current supplied, and gap size.

Figure 3.8 presents the relationship between both main variables from the previous equations (number of turns and current applied) using different gap sizes. Only the Equa-

tions 3.10 and 3.16 are plotted. The plane *magnetic length* = 0 ($z = 0$) shows the threshold where the magnetic length is negative. Any combination of values (number of turns per coil and current applied to the windings) below this plane cannot deliver the necessary magnetic flux density.

On the left column in Figure 3.8 a 1 mm gap size was used: figure a) plots the C-shape core while figure c) plots the E-shape core with one gap. There are more negative values than on the other figures. Knowing that a measured length is never a negative value, most of the results cannot be taken into consideration. The right column is calculated with a gap of 0.5 mm. The graphs show that there is no real minimum on the function (this can be seen on the equations, no quadratic term is found), that leaves the option to vary the values which are above the $z = 0$ plane on the graph.

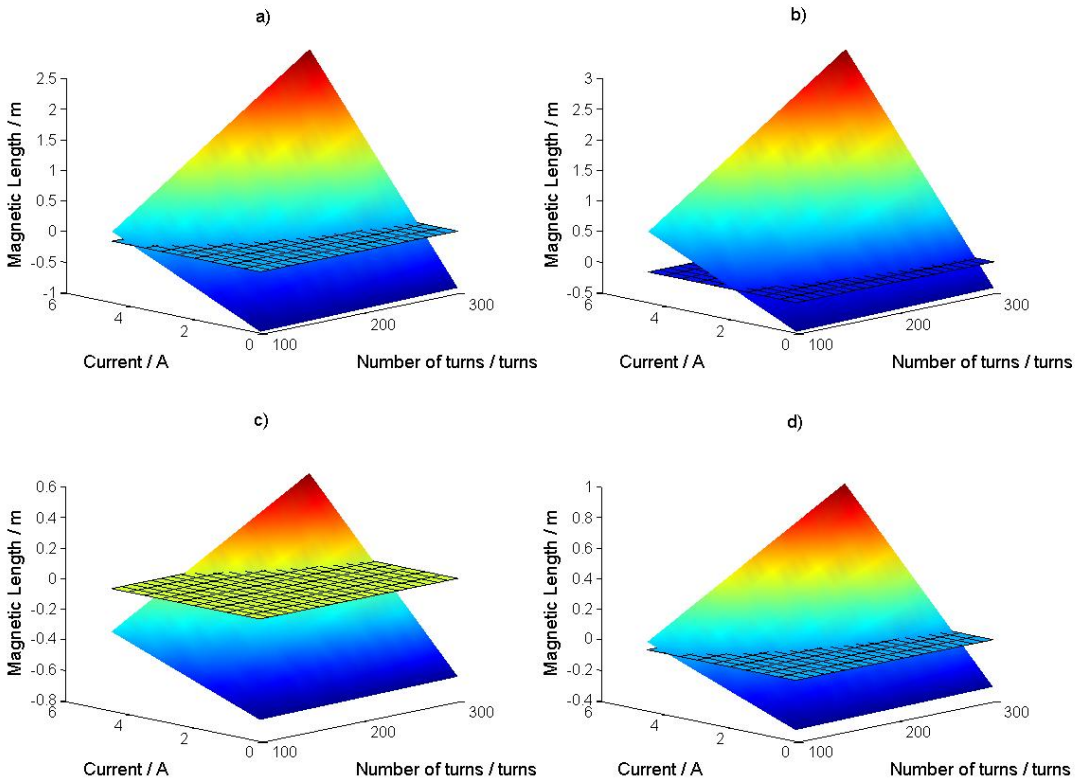

Figure 3.8: Plots representing the magnetic length of different core models, varying the number of turns , the current supplied and the gap size

The calculated results and some selected characteristics are shown in Table 3.1

Table 3.1: Parameters

Parameter	Value
Vacuum Permeability	$4\pi \times 10^{-7} H^{-1}$
Relative permeability of the magnetic core	1000
Relative permeability of the MSM material	2-3 on the Hard axis of magnetization, 50 on the easy axis
Gap size	0.5 mm
Number of turns	220 $turns$
Diameter of wire	0.8128 mm
Max amperage according following the recommendations of AWG	2.3 A
Required flux density on the material	1 T
Amperage required to generate 1 T	2 A
Mean length of the magnetic circuit	0.035 m

3.1.2 Geometry of the core

As stated in the Table 3.1, the maximum magnetic length to achieve the necessary field is 0.035 m or 35 mm. If the average length of the magnetic circuit is greater than this maximum value, the reluctance of the SiFe parts will be so high, that the required magnetic flux density will not be attained.

To define the thickness of the magnetic core, two things are considered: first, the MSM element must be magnetized on its whole length in order to obtain the highest reorientation; second, the pieces holding the MSM element in place should not interfere with the magnetic core. The pieces should remain in their place allowing the MSM element to elongate without any interference so that all the movement is transmitted to the final tip of the actuator.

Therefore a 12 mm-thick core is used: it will magnetize most of the MSM element (the length of the material used is 15 mm), and also the pieces that hold the MSM can be placed without a problem.

Using the diameter of the wire (to simulate the thickness of the varnish coating the copper wire an extra 10% is added to the diameter) and the number of turns, the space required to hold both coils in place is calculated.

$$Area_{conductor} = \frac{1}{4}\pi\varnothing^2 = \frac{1}{4}\pi[0.8128\ mm(1.1)]^2$$

$$Area_{conductor} = 0.06278\ mm^2 \tag{3.17}$$

To calculate the number of turns per unit area, the wire is visualized as a square. The area is calculated as $Area_{sqcond} = \varnothing^2 = [0.8128\ mm(1.1)]^2 = 0.799\ mm^2$. And then the no. of turns per unit area is

$$\text{Winding density} = Area_{sqcond}^{-1} = 1.25\ turns/mm^2$$

The required area (cross sectional area of one side of a coil) is calculated with the number of turns, and the winding density.

$$Area_{coil} = \frac{no.\ of\ turns}{winding\ density} = \frac{220\ turn}{1.25\ turns/mm^2} = 175.86\ mm^2$$

This area is now used to define the dimensions of the magnetic core. The legs (E-shape) were considered to have the same dimension. Using 7.5 mm as the width of the leg, the lengthof the coil is calculated.

$$inner\ length_{core} = \frac{175.86\ mm^2}{7.5\ mm} = 23.448\ mm$$

For the coils to be assembled on the actuator, a 1 mm-thick spool structure is used. This spool adds up to a total of 2 mm leading to an inner length of the core of 26 mm. The magnetic length does not surpass the one calculated before.

Figure 3.9 shows the overall dimensions of the core. The dotted line represents the magnetic length. All of the dimensions are in mm. In the following sections, the final design of the core will be shown.

3.2 Finite Element Analysis

To visualize the distribution of the magnetic field lines and validate the calculations and assumptions made in Section 3.1, a Finite Element Simulation was made. The selected

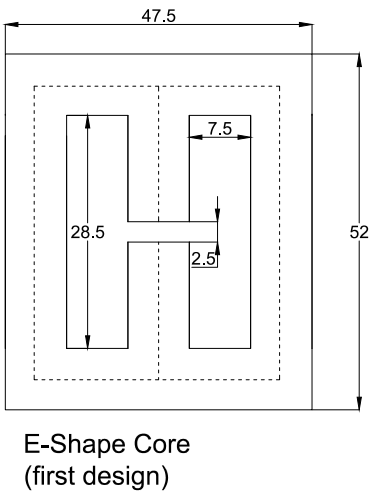

Figure 3.9: Basic dimensions of the core for FEM analysis.

software to perform the simulation, was *ANSYS APDL* (ANSYS Parametric Design Language).

In ANSYS, geometries (whether they are areas, lines, points or volumes) are meshed with different physical properties, so that elements can be formed and then loaded with input forces. Finally one can choose between plots or lists as an output for visualizing the results.

From the sections already mentioned, one can take the following data and add some more fields that will be used on the finite element model. The data is presented in Table 3.2.

3.2.1 2D Simulation

This first model was to observe and visualize the influence of the magnetic flux lines through the material. Also a first impression on how the magnetic field lines are arranged on the material can be obtained. In this first approach, a 2D drawing file was imported to *ANSYS* with all the surfaces required to mesh the model.

The first analysis was performed to check the geometry (tapered middle leg with the same width as the element -in this case 3 *mm*-) and the distribution of the magnetic flux density in the MSM element. In this first analysis the model is considered to be "plane". This means that the distribution of the field is uniform across thickness direction of the

Table 3.2: Properties for FEM analysis

Parameter	Value
Magnetic core	
Overall dimensions	$52 \times 47.5 \times 12\ mm^3$
Thickness of every sheet	$0.35\ mm$
B-H curve for the material	See corresponding table
Gap size	$0.5\ mm$
Windings	
Number of windings	2 units
Number of turns	$220\ turns$
Current per turn	$2\ A$
Cross-section area	$169\ mm^2$
MSM element	
Dimensions	$2\ \times 3\ \times 15\ mm^3$
Relative permeability	50 on Easy axis 2 on Hard axis

material (which in a 3d-model is not, one must consider the ends and fringe effects).

The sketch (later on converted to ANSYS model) can be seen in Figure 3.10.

The areas are meshed corresponding to the material model in ANSYS, so that all of the properties given before are assigned to the elements. The element size of every modelled area is selected based on the minimum space that separates areas in the model. For example, the area representing the air between both middle core legs and the MSM element, has an element size of 0.1 mm, while the outer part of the model has an element size of 1 mm. For the initial tests, an automatic sizing feature was selected.

After meshing the model with the corresponding material properties and the element size, the model was solved. The distribution of the field lines and the flux density in the MSM element can be seen in the next figures. In Figure 3.11 the element is acting as a "conductor" of the flux confirming the path the field lines will take in the real model.

In Figure 3.12 it can be seen that, although the necessary flux density in the material

Table 3.3: B-H curve of the iron material

H(A/m)	B(T)
0	0
2500	1.53
5000	1.64
10000	1.76

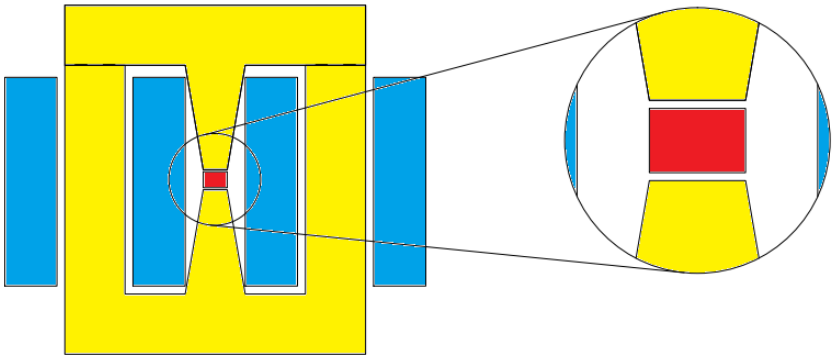

Figure 3.10: Sketch used for the ANSYS modelling. The colors represent the different materials used in the model: in red the MSM properties are loaded, in blue, current density as well as permeability of copper are added, on yellow the BH curve of the material is loaded.

is achieved, the gradients inside the element are quite high. This could mean that the material will not get the field distributed as planned, resulting in a diminished performance.

Because of this, different models were tested to improve the distribution of the flux density through the MSM element. Several models were tested with the same conditions, resulting in a more abruptly distributed field in the material. There was a model that could get the same magnitude of flux density in the material as well as providing an evenly distributed flux density. The results are presented in Figure 3.13

Since the 2D model got acceptable results, a 3D model was developed to visualise the distribution of flux density in the MSM element.

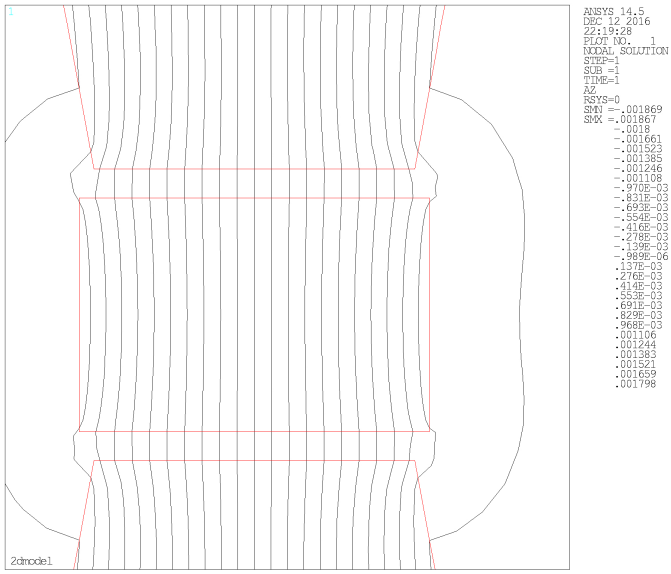

Figure 3.11: Magnetic field lines passing through the MSM element.

3.2.2 3D simulation

As stated in the previous section, the 3D model was used to see the 3D orientation and distribution of flux density in the material. Although the sketch used in 2D-modelling can be the base for a 3D model, a new model was developed to simulate the behaviour in a more precise way.

The set-up of the actuator is modelled with volumes, generated directly in the FEM software interface. As the previous model, volumes are meshed with material properties, element size, and real constants. This time the core, air and MSM elements form a part of the Finite Element Model. The difference is that the modelling of the coils changes; for this model, due to the scalar potential formulation, the coils are modelled as primitives. This means that they are not a part of the model as elements, but parameters added later on by the software.

The modelling of the coils as primitives, reduces number of nodes, thus reducing the computation time. For this model, two steps for simulation were taken: one to verify the amount of flux density generated without the MSM element and the second to verify the amount of flux density generated within the shape memory crystal.

The same magnetic properties as the previous 2D model are used in the 3D model to preserve the same conditions but yet to observe the 3D behaviour of it.

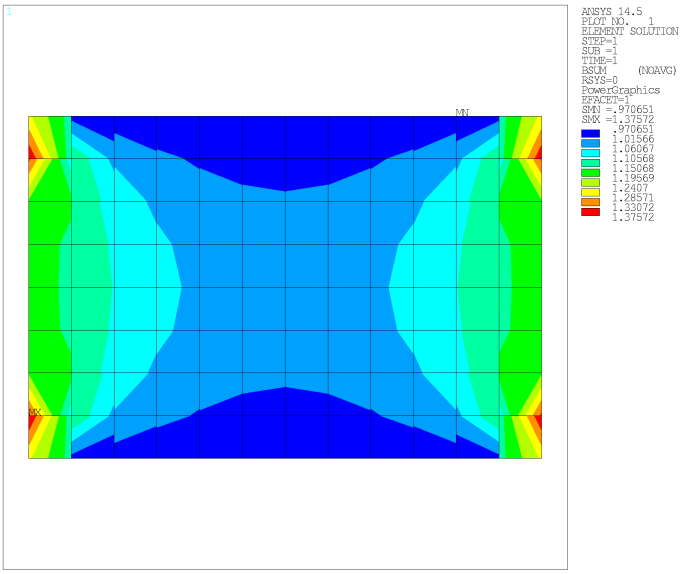

Figure 3.12: Magnetic flux density distribution in the MSM element for the first ANSYS model

Visualisation of flux density in air

These results were taken from the software to compare the calculations from Equation 3.15 and the measurements from the assembled core and coils.

Figure 3.14 represents the space contained between the inner faces of the SiFe core (the MSM volumes are given the properties of air for this simulation step only). Vector-representation form is used to visualise the solution better. The outline of this space can be seen in the figure.

From Figure 3.14, an average of 0.2 T is achieved which in agreement with the calculated value of 0.202 T and the measured flux density on the prototype $B_{max} = 0.187\ T$.

Visualisation of field on the MSM element

As predicted by the 2D model, the geometry of the core and the input values deliver the necessary magnetomotive force input to generate a field, on average, of 1 T on the element. Also the fringe effects on the end of the MSM element are visible. In Figure 3.15 the arrows represent the distribution of the flux density in the MSM element. On the ends of the prism (representing the MSM element in the figure), it can be seen that the tips of the MSM element will get a lower amount of flux density (blue arrows). This part of the MSM element, having a lower flux density, may not get enough excitation to induce a

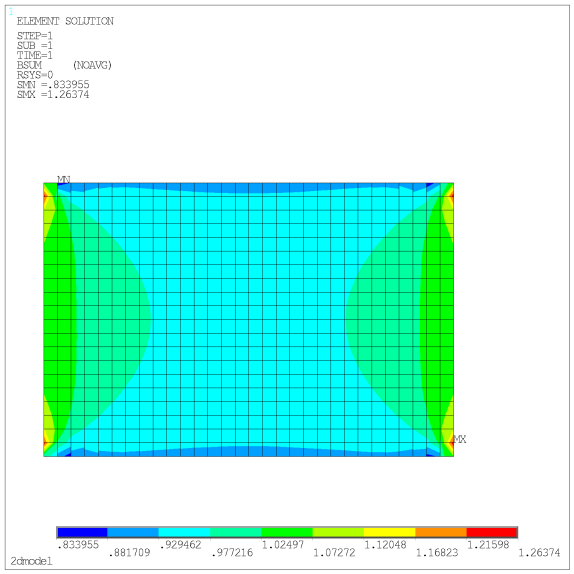

Figure 3.13: Magnetic flux density distribution in the MSM element for the improved model

change on the crystalline structure.

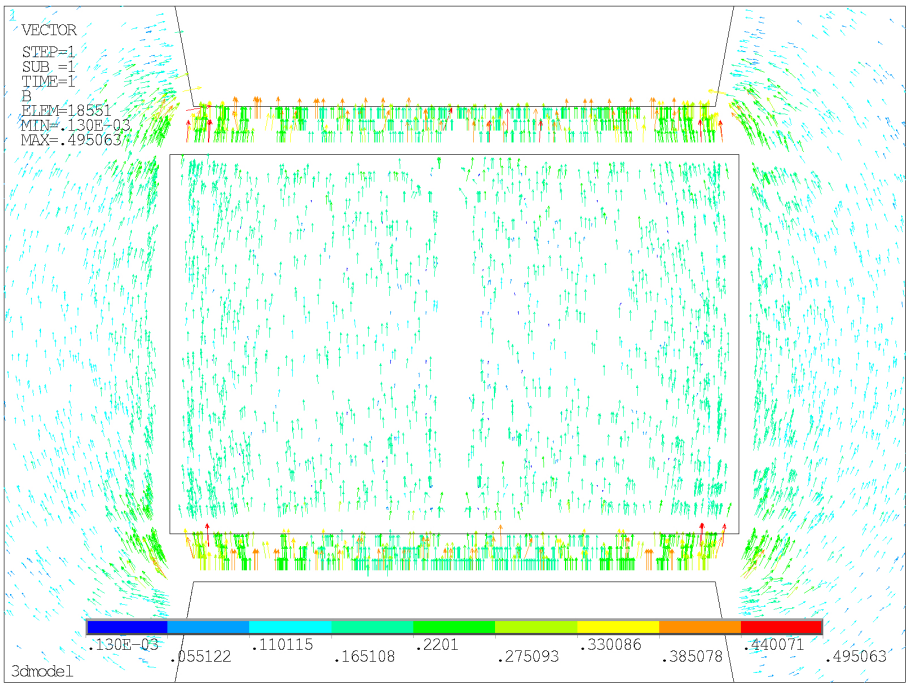

Figure 3.14: Representation of the B field of the 3D model of the core without the MSM element volumes

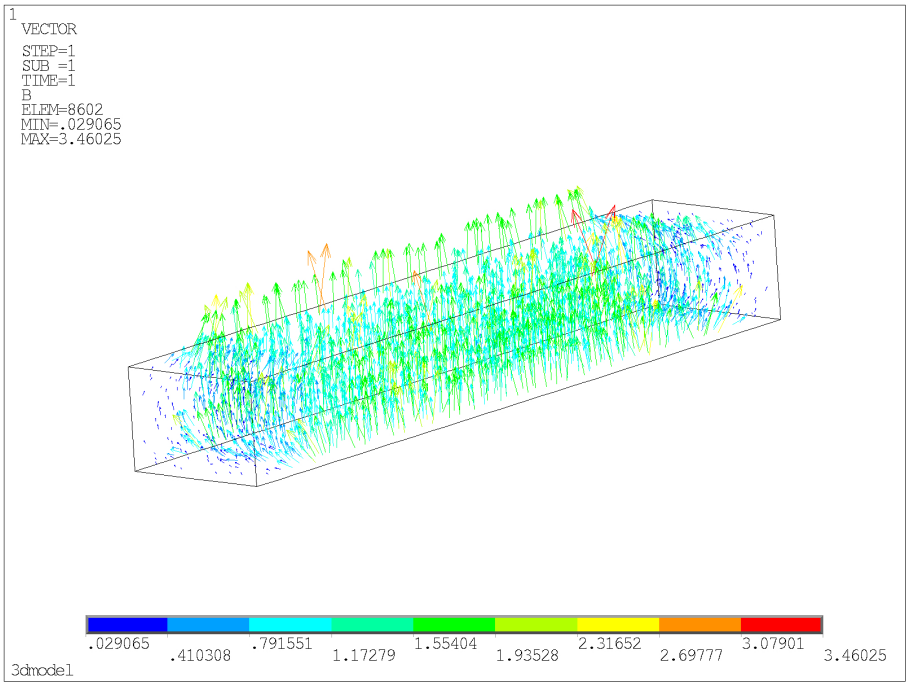

Figure 3.15: Vector representation of distribution of the field on the material labeled as MSM.

Chapter 4

Sensors

In this phase of development of the actuator, the first set-up was designed to contain the minimum sensors to quantify the characteristics of the actuator, such as strain, compressing stress applied on the MSM and the field generated by the coils. Measuring schemes were developed to measure each quantity.

For measuring the magnetic field, a Hall probe is placed in the gap of the magnetic core. This data helps evaluate the magnetic behaviour of the core.

Both distance and force sensors measurement were done while testing the complete assembly of the actuator.

The force sensor measures the counter force applied on the MSM element; the distance sensor on the other hand, measures the displacement of the tip of the actuator. These measurements, together give out some of the main features of the actuator.

The actuator is placed on a flat and steady surface and the tip of the actuator faces the distance sensor. The force sensor is embedded in the assembly of the actuator.

On the following sections a brief description of the mode of operation of the sensors is presented as well as the way to obtain the data.

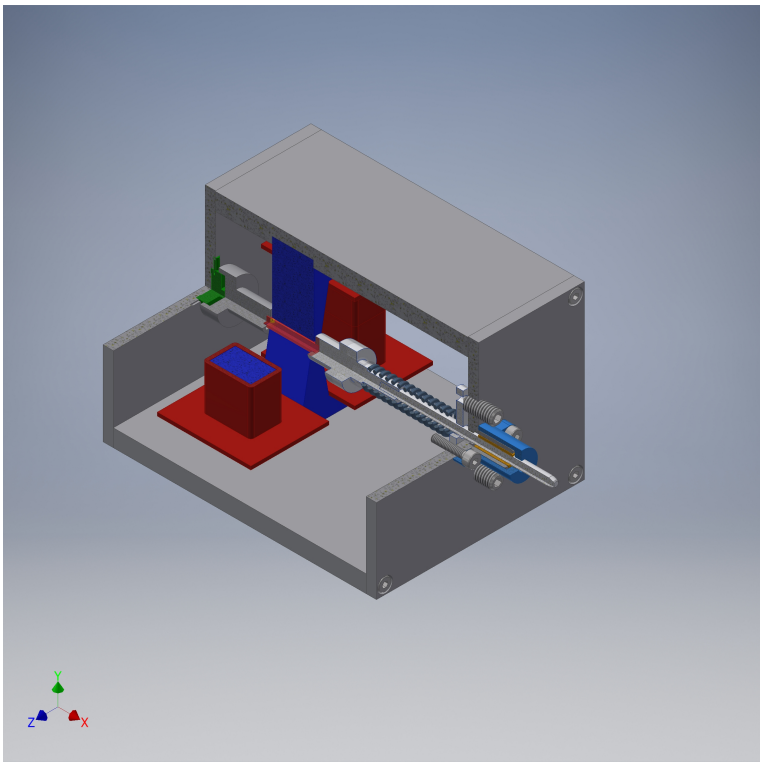

Figure 4.1: Final assembly of the actuator, the force sensor is located on the back side of the actuator (green). The distance sensor is not shown

4.1 Distance Sensor

For measuring the stroke of the actuator a distance sensor is used. Contact type sensors are not considered. Only non-contact sensors are considered because they do not interfere with the stroke generated by the MSM material. Sensors based on inductive, capacitive, Hall effect and laser-based were considered. A laser triangulation distance sensor was selected because of its high accuracy and high resolution.

Laser triangulation sensors follow the principle of light reflection. An incident laser will be reflected by the surface to measure. The intensity of the reflected beam is measured by the sensor, and with some calculations considering the intensity and angle of incidence of this beam, the distance between the projected beam and the surface is calculated.

The laser sensor optoNCDT 1302-20 from Micro-Epsilon was selected. It has a resolution of 40 μm and it works based on laser triangulation.

Some of the most important features are shown on the Table 4.1

Table 4.1: Laser sensor Characteristics

Feature	Value
Measuring range	$30 - 50\ mm$
Resolution max	$40\ \mu m$
Linearity	$40\ \mu m$
Input voltage	$11 - 30\ V$
Output (analog)	$4 - 20\ mA$
Output (analog voltage)	$R_{load} = 250\ \Omega \quad U_{out} = 1 - 5\ V$

The analog current output of this sensor varies between $4 - 20\ mA$ depending on the distance. To acquire the data with a Data Acquisition Card (DAQ), the current must be converted into a voltage. A shunt resistor was used with a DAQ to convert current into voltage.

Figure 4.2: Laser sensor used on the prototype optoNCDT 1302-20 from Micro-Espilon [21]

4.2 Force Sensor

For this application (mode of operation) the force sensor is required to check the pre-stress applied by the spring. The requirements for this sensor are:

- Easy to mount.
- Not affected by magnetic fields.
- Easy to measure output.
- Capability to withstand overload.
- Small package.
- Low deflection upon applied force.

Accounting for the previous requirements, the force sensor *KM-10* $25N$ from ME-Meßsysteme was selected. This sensor is based on piezoresistive materials. Piezoresistive effect is the change of electrical resistivity when the material experiences mechanical stress.

KM-10 $25N$ is configured as a full Wheatstone bridge where four sensing resistances are used. The full Wheatstone bridge is highly sensitive and helps minimize temperature errors. Using the formulae for a Wheatstone bridge, the output depends on the voltage applied on the input side and the force applied on the tip of the sensor.

Table 4.2 compiles some of the characteristics of the sensor.

Table 4.2: Force sensor Characteristics

Feature	Value
Dimensions	$\varnothing$ 9.8×4 mm
Full Scale (FS)	25 N
Operating Force	$150\% FS$
Zero signal output	0.1 mV/V
Rated Displacement	0.08 mm
Rated range input voltage	$2.5 - 5$ V
Characteristic value range	$0.5 - 1.1$ mV/V

4.2.1 Instrumentation amplifier

Due to the fact that the force sensor gives out a very small signal, even the smallest RF interference can affect the data acquired by the designed program. For this reason, an

instrumentation amplifier was designed and used to avoid the RF interference. A software based filter was applied in LabVIEW, reducing the noise in the measured signal.

The selection of the amplifier was based on three aspects: output offset, possible "programmable" gain (adjustable with an external resistor so that this amplifier can be interchangeable) and power consumed. There are many instrumentation amplifiers on the market which can provide almost a zero-volt output. For this prototype of actuator, one must first prove that the behaviour of the entire project satisfies the expected characteristics. With this in mind, cost is one of the strongest points to consider on the selection of the instrumentation amplifier. *Analog Devices* provides a wide range of instrumentation amplifiers on different packaging (SOIC,DIP): this devices can be considered cheap as a "precise" amplifier can cost around 100 €. For this reason one cheap amplifier with low output voltage offset is selected: the Analog Devices instrumental amplifier AD620. The only drawback of this amplifier is that it must be provided with a bipolar voltage source, this implies that the actuator will need an extra voltage source or circuit to operate on negative voltage values. But this drawback is surpassed by the fact that the sensor can get a no load signal on a negative voltage level.

In order to connect the amplifier and also to provide the necessary voltage to the piezoresistive sensor, a printed circuit board was designed to hold all the components in place on a final stand. In Figure 4.3 the schematic of the electronic circuit can be seen.

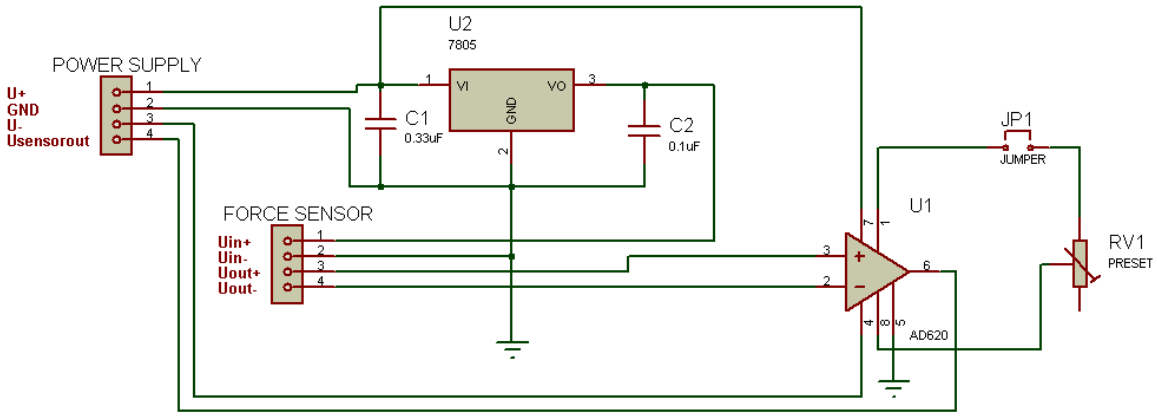

Figure 4.3: Schematics for the regulation of the supplied voltage of the force sensor and the instrumentation amplifier

In order to verify the characteristics of the force sensor, a program was developed to acquire and compare the data from the force and laser sensor. Also a small set-up was

built where the force applied to the sensor was calculated by using a spring with known spring constant. This set-up was used to measure the offset of the zero-force output signal, and the gain of the sensor. In this case the selected units to represent the gain of the sensor are Newton/Volt (N/V).

The procedure is described as follows: the sensor was placed where almost no electromagnetic interference happens and no load was applied, then a sample of several seconds was taken. The second part of the experiment consists of applying a force with the spring and measuring three positions. The voltages given by the shunt resistor on the laser distance sensor are then saved in a file as well as the voltages given from the force sensor.

After the measurements were completed, the sensitivity of the sensor was obtained. This value was compared with the one provided by the calibration protocol of the manufacturer, the magnitude was almost the same as the one measured. Therefore it can be said that the data acquired from the program matches the datasheet.

To obtain the gain of the sensor, the average values of the measurements after filtering were taken (with little noise the mean value of the collection can be a representative indicator of the real value) and manipulated as follows.

$$G_d = \frac{range_v}{range_d} \tag{4.1}$$

$$\Delta d = \frac{\Delta V_d}{G_d} \tag{4.2}$$

$$G_f = \frac{\Delta d \; k}{\Delta V_f} \tag{4.3}$$

where:
G_d is the gain of the laser distance sensor $[V/mm]$
$range_v$ is the output range of the laser distance sensor $[V]$
$range_d$ is the difference between maximum and minimum distance the sensor can measure $[mm]$
Δd is the variation of distance $[mm]$
ΔV_d is the difference in voltage of the distance sensor $[V]$
G_f is the gain of the force sensor $[N/V]$

Figure 4.4: Gaussmeter used to measure the magnetic field

k is the spring constant used $[N/mm]$
ΔV_f is the difference in voltage of the force sensor $[V]$

The results of this collection of data are shown on Table 4.3. The zero signal output is positive because of the offset given by the amplifier.

Table 4.3: Verification of Force sensor calibration data

Description	Value
Zero output	$0.015V$
Operating voltage	$4.95\ V$
Gain of the sensor	$13\ N/V$

4.3 Gaussmeter

For measuring the magnetic field in the magnetic core the Lakeshore DSP 475 Gaussmeter was used. Digital Signal Processing technology creates a solid foundation for accurate, stable, and repeatable field measurement while simultaneously enabling the gaussmeter to offer an unequaled set of useful measurement features [22].

The main features of this measuring instrument are:

- Full-scale ranges from 35 mG to 350 kG

- DC measurement resolution to 0.02 mG
- Basic DC accuracy of $\pm 0.05\%$
- DC to 50 kHz frequency range (probe-dependent)
- 15 band-pass and 3 low-pass AC filters

The available Hall probes are classified by how they measure magnetic field: axially or transversally. Also the probes are organized by the frequency of the magnetic field the user would like to measure. For measuring the magnetic field, the probe model HMNT-4E04-VR will be used. This probe measures magnetic field normal to the thickness direction. This is convenient due to the small space where the probe should placed.

Chapter 5

Data acquisition and Results

After the calibration of the sensor and first set-up of the prototype, a program was developed to control the power supply and to acquire the data from the sensors.

For this task a computer program was made to perform the measurements in an automatic way. One only should adjust the first values of calibration, and the program would do the measurements automatically. Also the program itself can keep a log of the data which later will be useful for discussing the characteristics of the sensor.

5.1 Labview code

LabVIEW from National Instruments is a graphical programming language used to facilitate the development of widgets, applications and similar tasks. It is intended for scientists and engineers and helps them automating tasks, measuring sets of data, data processing, and so on.

This section briefly describes how the code is implemented to obtain data and check for the behaviour of the prototype.

First of all, the configuration controls are set so that the tasks on LabVIEW can be changed whenever the user wants to change them. This includes among others: physical channel, terminal configuration (differential, pseudodifferential, floating, etc), file path, sampling rate and number of samples per loop.

Some clusters gather similar data (current values, MSM element dimensions, force and distance sensors characteristics) which are used in the code for calculations.

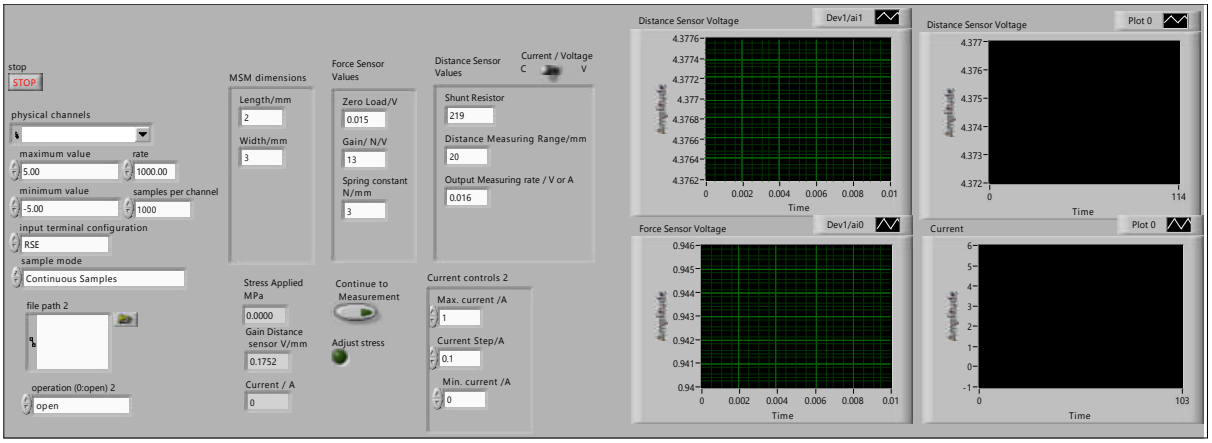

Figure 5.1: Front panel of the LabVIEW code

Indicators on the front panel show values that can be useful for the users. In this case, the compressive stress at which the material is put through is shown and also the ongoing electrical current passing through the coils.

Live fed charts are added so that measurements are seen as they are acquired from the acquisition card. These charts represent the actual current applied to the coils and the distance of the tip of the actuator.

For using the program these steps are followed: first make sure that the configuration values of the program are correctly filled out. After that a flashing indicator will tell the user that the pre-stress of the material can be adjusted. The user can see the actual stress being applied on the MSM on a numeric indicator located on the front panel.

After this step, the user presses one button and the loop will start automatically. At the end of the loop, the user will be shown the data collected for future analysis.

5.2 Results

In previous chapters the actuator was described from the development of the magnetic circuit, the selection of the sensors, and finally the code needed to obtain the data that

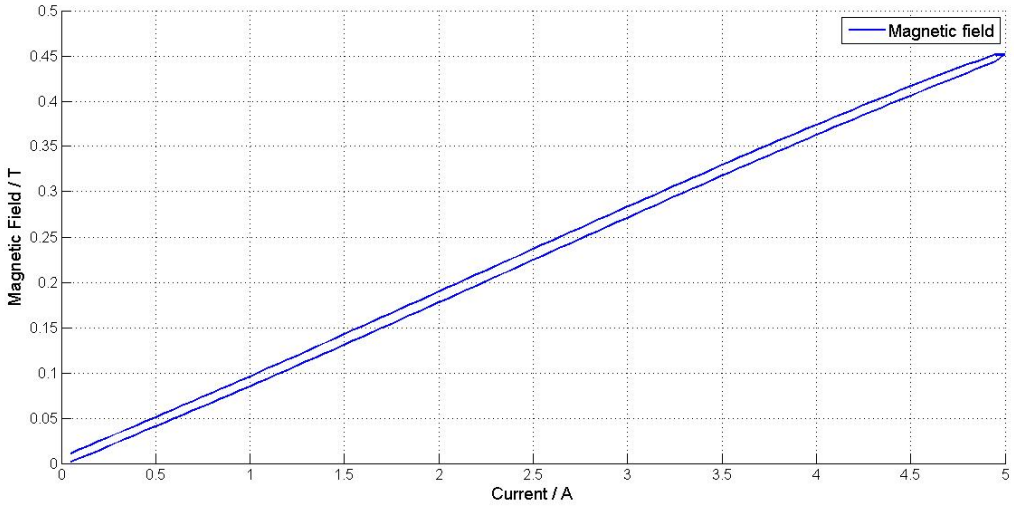

Figure 5.2: Graphic with the magnetic field generated on the gap (2.5 mm)

represents the actuator.

The following results were saved in the form of a *.tdms* file, native to LabVIEW. Some of this data is presented later on this section.

Two different tests were carried out: one to measure the magnetic field that can be generated on the MSM element, and the other measuring the distance with different applied magnetic fields. This two tests were not performed simultaneously due to the limitation of space between the MSM element and the SiFe core. The hall probe used on the gaussmeter has a thickness in the measuring direction of 1.14 mm while the maximum distance (due to design) between the MSM and the core is about 0.5 mm.

In the first test, the core and coils were fed with a ramp current signal. The generated magnetic field was measured using the gaussmeter and the data was stored in a file.

Although in Figure 5.2 the curve behaves as if the material is working in the linear region of the BH-curve, it should be noted that this test is performed with a larger gap size.

Then the second test is performed to characterise the designed actuator. The actuator was set up on an aluminium stand to keep it as steady as possible. The coils were fed with a ramp-current source taking small steps, defined by the user. The data was saved in a .tdms file. The program in Figure 5.1 waits for the user to manually adjust the mechanical

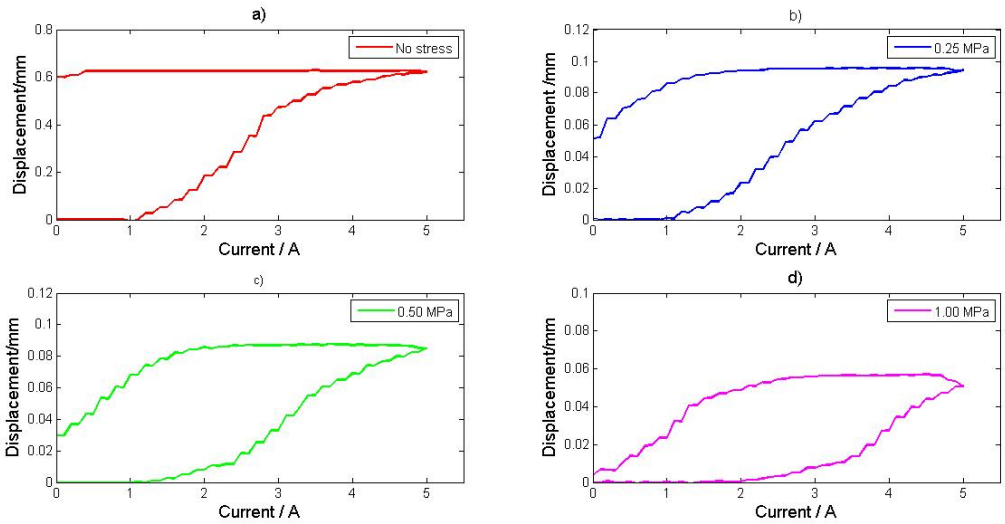

Figure 5.3: Characteristic curves of actuator appliying different amount of pre-stress

stress on the MSM. After adjusting the stress, the user can press the button on the front panel and automatically the ramp is generated as well as the data acquisition.

To present the results, the files were processed to plot them on charts. The results are shown in Figure 5.3.

In the subfigure a), no mechanical pre-stress is applied. The initial position is taken with the MSM in a "compressed state" and the current is applied slowly, taking measurements, of both force and distance sensor. In the same figure, the hysteresis behaviour of the actuator can be observed, which is due to the internal stress (twinning stress). The magnetic stress generated by the magnetic field must surpass this threshold level in order for the twin variants to move. Once all the possible twin variants have aligned to the magnetic field, the material remains in the same shape even after switching the magnetic field off .

From subfigures b) to d), a pre-stress is applied with a loaded spring. The compression of the spring is achieved by adjusting two screws on the outer part of the actuator. The resulting stress on the material depends on the compression of the spring.

The same basic shape (like in subfigure 5.3 a)) is achieved, but now the elongation of the material is reduced significantly. The stroke of the actuator is dependant on the pre-stress applied to the material: the higher the pre-stress, lesser the stroke one can get from the actuator. In addition, the material returns to the original shape faster when a

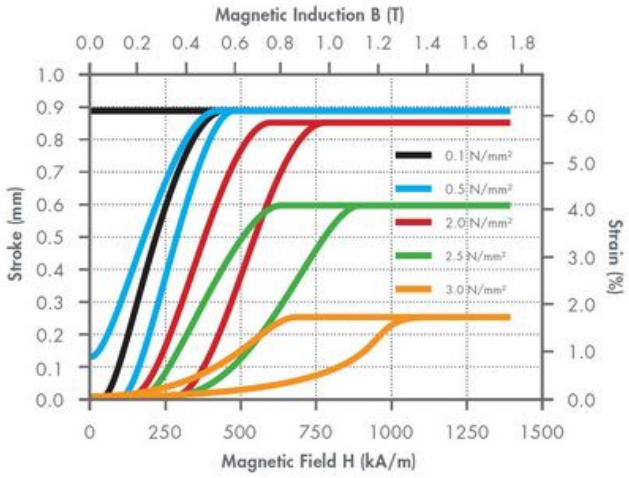

Figure 5.4: ETO Gruppe technical data

higher mechanical stress is applied to the material.

In comparison with the results provided by ETO Gruppe, [19] this model does not provide the 6% strain without mechanical stress. This can be explained by the fact that the crystal is not receiving enough orthogonal magnetic field lines. If the material is not receiving enough flux density, not all of the twin structures in the crystal will switch. One solution to this problem, is to design a better holding element for the MSM element. This element should hold the MSM in place and also allow the MSM to receive a magnetic field on its entire length.

In this first attempt of MSM-spring actuator, the returning force was provided by the spring. This spring has a relative high spring constant (3 N/mm), this affect the final measurements of stroke: the pre-stress should be manually adjusted every time this becomes too high. But if a spring with a low spring constant is used, the difference in stress between the relaxed and the excited state of the MSM will not be too high. This solution can eliminate the need to adjust the stress manually, in consequence, the process of characterisation can be done almost automatically.

Chapter 6

Conclusions and future works

6.1 Conclusions

In this thesis, the design of the a magnetic shape memory alloy actuator was addressed as the main objective. The main contribution made during the completion of this thesis is the construction of a functional MSM actuator based on the second mode of operation. After the experiments were done, advantages, disadvantages and obstacles of this mode of operation were discussed.

The mathematical model of the cores were also provided to support the development of this actuators. Even tough they are made with some simplifications and idealisations they represent at certain level the behaviour of the model.

Finite element model simulations also were made. These Finite Element models are also included in this thesis as a baseline for the reader to become familiarised with the simulation of magnetic circuits.

The static characteristics of the actuator were provided as well as the data generated from the sensors during the execution of the experiments described.

Overall speaking, this thesis have provided the basis to continue to work on this exciting new kind of materials. The smart materials soon will be part of our life in ways we cannot imagine yet. Their properties give engineers and scientists a whole panorama to develop new kind of actuators.

6.2 Future work

For oncoming works that can be done regarding MSM materials, one can design other test stands, using a different mode of operation. Also one can design another kind of actuator based on the ones given on previous sections.

While the static characteristics of this actuator were determined, the dynamic properties of this actuator were not contemplated due to lack of time. New tests and experiments should be prepared in order to measure the whole characteristics of the actuator for it to be fully characterised.

The most important task when using an actuator on an automated process is the ability to control the output variable of it. In the present thesis no control method was devised for the stroke of the actuator. This can be an excellent opportunity for a control system to be designed for controlling the stroke of the actuator.

Finally the program used can be upgraded to include more modes of actuations, different configurations of actuators, or even add features such as measuring of the dynamic characteristics of the actuator.

Bibliography

[1] K. Ullakko. Magnetically controlled shape memory alloys: A new class of actuator materials. *Journal of Materials Engineering and Performance*, 5(3):405–409, jun 1996.

[2] Manfred Kohl, Marcel Gueltig, Viktor Pinneker, Ruizhi Yin, Frank Wendler, and Berthold Krevet. Magnetic shape memory microactuators. *Micromachines*, 5(4):1135–1160, 2014.

[3] S.R. Yeduru, A. Backen, S. Fähler, L. Schultz, and M. Kohl. Transformation behaviour of freestanding epitaxial Ni-Mn-Ga films. *Journal of Alloys and Compounds*, 577:S353–S357, nov 2013.

[4] W. M. Huang, Z. Ding, C. C. Wang, J. Wei, Y. Zhao, and H. Purnawali. Shape memory materials. *Materials Today*, 13(7-8):54–61, 2010.

[5] Peter Entel, Vasily D. Buchelnikov, Markus E. Gruner, Alfred Hucht, Vladimir V. Khovailo, Sanjeev K. Nayak, and Alexey T. Zayak. Shape Memory Alloys: A Summary of Recent Achievements. *Materials Science Forum*, 583:21–41, 2008.

[6] Takuo Sakon, Yoshiya Adachi, and Takeshi Kanomata. Magneto-Structural Properties of Ni_2MnGa Ferromagnetic Shape Memory Alloy in Magnetic Fields. *Metals*, 3:202–224, 2013.

[7] Hane, Kevin F. Twinned Martensite. `http://www.aem.umn.edu/~shield/hane/micro.twin.html`. Online.

[8] Thomas Schiepp, Manuel Maier, Emmanouel Pagounis, Andreas Schluter, and Marku Laufenberg. FEM-Simulation of Magnetic Shape Memory Actuators. *IEEE Transactions on Magnetics*, 50(2):989–992, feb 2014.

[9] A. Sozinov, A. A. Likhachev, and Kari Ullakko. Crystal structures and magnetic anisotropy properties of Ni-Mn-Ga martensitic phases with giant magnetic-field-induced strain. *IEEE Transactions on Magnetics*, 38(5 I):2814–2816, 2002.

[10] Benedikt Holz, Leonardo Riccardi, Hartmut Janocha, and David Naso. MSM actuators: Design rules and control strategies. *Advanced Engineering Materials*, 14(8):668–681, 2012.

[11] B. Kiefer and D. C. Lagoudas. Magnetic field-induced martensitic variant reorientation in magnetic shape memory alloys. *Philosophical Magazine*, 85(33-35):4289–4329, 2005.

[12] S. Fähler. Why Magnetic Shape Memory Alloys? *Advanced Engineering Materials*, 14(8):521–522, aug 2012.

[13] B Minorowicz, A Nowak, and F Stefański. Position regulation of magnetic shape memory actuator. *Journal of Achievements in Materials and Manufacturing Engineering*, 61(2):216–221, 2013.

[14] K Majewska, a Zak, and W Ostachowicz. Magnetic Shape Memory (MSM) actuators in practical use. *Journal of Physics: Conference Series*, 181:012073, 2009.

[15] Adaptamat. Magnetic shape memory (MSM) Technology. `http://www.prizz.fi/sites/default/files/tiedostot/linkki2ID924.pdf`. Online.

[16] Boise State University. Magnetic Shape Memory Micro-Pump for IntraCranial Drug Delivery. `http://scholarworks.boisestate.edu/cgi/viewcontent.cgi?article=1032&context=eng_14`. Online.

[17] Kathrin Schlüter, Benedikt Holz, and Annika Raatz. Principle design of actuators driven by magnetic shape memory alloys. *Advanced Engineering Materials*, 14(8):682–686, 2012.

[18] E. Pagounis, A. Laptev, J. Jungwirth, M. Laufenberg, and M. Fonin. Magnetomechanical properties of a high-temperature Ni-Mn-Ga magnetic shape memory actuator material. *Scripta Materialia*, 88:17–20, 2014.

[19] ETO Gruppe. Magnetoshape. `http://etogroup.com/MAGNETOSHAPE_EN.html`. Online.

[20] P. Müllner, V. A. Chernenko, and G. Kostorz. A microscopic approach to the magnetic-field-induced deformation of martensite (magnetoplasticity). *Journal of Magnetism and Magnetic Materials*, 267(3):325–334, 2003.

[21] Micro-epsilon. Laser triangulation laser sensors. `http://www.micro-epsilon.com/displacement-position-sensors/laser-sensor/standard-sensors-1302_1402/index.html`. Online.

[22] Lakeshore Cryotronics. Model 475 DSP Gaussmeter. `http://www.lakeshore.com/products/Gaussmeters/Model-475-DSP-Gaussmeter/Pages/Overview.aspx`. Online.

Appendix A

Ansys model

Here the commands necessary to generate the models on ANSYS are presented. The section A.1 the geometries are imported from a drawing file. On section A.2 the model is generated entirely on commands.

A.1 2D model

```
    /PREP7
!*
/NOPR
KEYW,PR_ SET,1
KEYW,PR_ STRUC,0
KEYW,PR_ THERM,0
KEYW,PR_ FLUID,0
KEYW,PR_ ELMAG,1
KEYW,MAGNOD,1
KEYW,MAGEDG,0
KEYW,MAGHFE,0
KEYW,MAGELC,0
KEYW,PR_ MULTI,0
KEYW,PR_ CFD,0
/GO
!*
! /COM,
!  /COM,Preferences for GUI filtering have
been set to display:
! /COM, Magnetic-Nodal
!*
!*
ET,1,SOLID96
!*
!*
TB,BH,1,1,4,
TBPT,,0,0
TBPT,,2500,1.53
TBPT,,5000,1.64
TBPT,,10000,1.76
```

```
MPTEMP,,,,,,,,
MPTEMP,1,0
MPDATA,MURX,1,,1
MPDE,MURX,1
MPTEMP,,,,,,,,
MPTEMP,1,0
MPDATA,MURX,2,,1
MPTEMP,,,,,,,,
MPTEMP,1,0
MPDATA,MURX,3,,50
FLST,2,8,5,ORDE,2
FITEM,2,9
FITEM,2,-16
AOVLAP,P51X
FLST,2,9,5,ORDE,5
FITEM,2,1
FITEM,2,-3
FITEM,2,10
FITEM,2,12
FITEM,2,-16
AOVLAP,P51X
FLST,2,9,5,ORDE,8
FITEM,2,0
FITEM,2,0
FITEM,2,0
FITEM,2,-2
FITEM,2,2
FITEM,2,-3
FITEM,2,7
FITEM,2,62
AOVLAP,P51X
FLST,5,6,5,ORDE,4
FITEM,5,2
FITEM,5,-3
FITEM,5,13
FITEM,5,-16
CM,_Y,AREA
ASEL, , , ,P51X
CM,_Y1,AREA
CMSEL,S,_Y
CMSEL,S,_Y1
AATT, 2, , 1, 0,
CMSEL,S,_Y
CMDELE,_Y
CMDELE,_Y1
CM,_Y,AREA
ASEL, , , , 10
CM,_Y1,AREA
CMSEL,S,_Y
CMSEL,S,_Y1
AATT, 3, , 1, 0,
CMSEL,S,_Y
CMDELE,_Y
CMDELE,_Y1
FLST,2,2,5,ORDE,2
FITEM,2,3
FITEM,2,10
FLST,2,1,5,ORDE,1
FITEM,2,10
AESIZE,P51X,0.1,
FLST,2,1,5,ORDE,1
FITEM,2,3
AESIZE,P51X,0.25,
MSHKEY,0
FLST,5,9,5,ORDE,5
FITEM,5,1
FITEM,5,-3
FITEM,5,10
FITEM,5,12
FITEM,5,-16
CM,_Y,AREA
ASEL, , , ,P51X
```

```
CM,_Y1,AREA
CHKMSH,'AREA'
CMSEL,S,_Y
AMESH,_Y1
CMDELE,_Y
CMDELE,_Y1
CMDELE,_Y2
ET,1,PLANE233
MSHKEY,0
FLST,5,9,5,ORDE,5
FITEM,5,1
FITEM,5,-3
FITEM,5,10
FITEM,5,12
FITEM,5,-16
CM,_Y,AREA
ASEL, , , ,P51X
CM,_Y1,AREA
CHKMSH,'AREA'
CMSEL,S,_Y
AMESH,_Y1
CMDELE,_Y
CMDELE,_Y1
CMDELE,_Y2
FLST,2,4,4,ORDE,2
FITEM,2,5
FITEM,2,-8
DL,P51X, ,ASYM
FLST,2,2,5,ORDE,2
FITEM,2,13
FITEM,2,-14
BFA,P51X,JS, , ,2600000,0
FLST,2,2,5,ORDE,2
FITEM,2,13
FITEM,2,15
BFA,P51X,JS, , ,2600000,0
FLST,2,2,5,ORDE,2
FITEM,2,14
FITEM,2,16
BFA,P51X,JS, , ,-2600000,0
FLST,2,9,5,ORDE,5
FITEM,2,1
FITEM,2,-3
FITEM,2,10
FITEM,2,12
FITEM,2,-16
ARSCALE,P51X, , ,0.001,0.001,1, ,0,1
FINISH
/POST1
FINISH
/SOL
! /STATUS,SOLU
SOLVE
FINISH
```

A.2 3D model

```
   /NOPR
KEYW,PR_SET,1
KEYW,PR_STRUC,0
KEYW,PR_THERM,0
KEYW,PR_FLUID,0
KEYW,PR_ELMAG,1
```

```
KEYW,MAGNOD,1
KEYW,MAGEDG,0
KEYW,MAGHFE,0
KEYW,MAGELC,0
KEYW,PR_MULTI,0
KEYW,PR_CFD,0
/GO
! /COM,
! /COM,Preferences for GUI filtering have been set to display:
! /COM, Magnetic-Nodal
/PREP7
ET,1,SOLID96
ET,2,SOURC36
TB,BH,1,1,4,
TBPT,,0,0
TBPT,,2500,1.53
TBPT,,5000,1.64
TBPT,,10000,1.76
MPTEMP,,,,,,,,
MPTEMP,1,0
MPDATA,MURX,2,,1
MPTEMP,,,,,,,,
MPTEMP,1,0
MPDATA,MURX,3,,3
MPDATA,MURY,3,,50
MPDATA,MURZ,3,,50
wpoff,25,25,25
CSYS,0
WPAVE,0,0,0
CSYS,0
wpoff,0.025,0.025,0.025
BLOCK,0,0.0375,0, 0.012,0,0.0435,
BLOCK,0,0.0375,0, 0.012,0,0.0075,
BLOCK,0,0.0075,0, 0.012,0,0.0435,
FLST,3,1,6,ORDE,1
FITEM,3,2
VGEN,2,P51X, , ,0,0,0.036, ,0
FLST,3,1,6,ORDE,1
FITEM,3,3
VGEN,2,P51X, , ,0.03,0,0, ,0
BLOCK, 0.01725, 18.75/1000, -0.0015, 0.0135, 20.75/1000, 0.02275,
BLOCK, 0.01875, 20.25/1000, -0.0015, 0.0135, 20.75/1000, 0.02275,
wpoff,0.015,0,0.0075
FLST,3,1,8
FITEM,3,0.4E-01,0.25E-01,0.325E-01
K, ,P51X
FLST,3,1,8
FITEM,3,0.4E-01,12.025,0.325E-01
K, ,P51X
KDELE, 58
FLST,3,1,8
FITEM,3,0.4E-01, 0.37E-01,0.325E-01
K, ,P51X
FLST,3,1,8
FITEM,3,0.475E-01, 0.25E-01,0.325E-01
K, ,P51X
FLST,3,1,8
FITEM,3,0.475E-01, 0.37E-01,0.325E-01
K, ,P51X
wpoff,0.002375,0,0.013
FLST,3,1,8
FITEM,3, 0.42375E-01, 0.25E-01, 0.455E-01
K, ,P51X
FLST,3,1,8
FITEM,3, 0.42375E-01, 0.37E-01, 0.455E-01
K, ,P51X
FLST,3,1,8
```

```
FITEM,3, 0.45125E-01, 0.25E-01, 0.455E-
01
K, ,P51X
FLST,3,1,8
FITEM,3, 0.45125E-01, 0.37E-01, 0.455E-
01
K, ,P51X
FLST,3,4,3,ORDE,2
FITEM,3,57
FITEM,3,-60
KGEN,2,P51X, , ,0,0,0.0285, ,0
FLST,3,4,3,ORDE,2
FITEM,3,61
FITEM,3,-64
KGEN,2,P51X, , ,0,0,0.0025, ,0
FLST,2,4,3
FITEM,2,60
FITEM,2,58
FITEM,2,57
FITEM,2,59
A,P51X
FLST,2,4,3
FITEM,2,58
FITEM,2,62
FITEM,2,61
FITEM,2,57
A,P51X
FLST,2,4,3
FITEM,2,61
FITEM,2,63
FITEM,2,64
FITEM,2,62
A,P51X
FLST,2,4,3
FITEM,2,61
FITEM,2,57
FITEM,2,59
FITEM,2,63
A,P51X
FLST,2,4,3
FITEM,2,64
FITEM,2,60
FITEM,2,59
FITEM,2,63
A,P51X
FLST,2,4,3
FITEM,2,64
FITEM,2,60
FITEM,2,58
FITEM,2,62
A,P51X
FLST,2,4,3
FITEM,2,69
FITEM,2,71
FITEM,2,72
FITEM,2,70
A,P51X
FLST,2,4,3
FITEM,2,71
FITEM,2,67
FITEM,2,65
FITEM,2,69
A,P51X
FLST,2,4,3
FITEM,2,65
FITEM,2,66
FITEM,2,70
FITEM,2,69
A,P51X
FLST,2,4,3
FITEM,2,67
FITEM,2,71
```

```
FITEM,2,72
FITEM,2,68
A,P51X
FLST,2,4,3
FITEM,2,66
FITEM,2,68
FITEM,2,67
FITEM,2,65
A,P51X
FLST,2,4,3
FITEM,2,66
FITEM,2,70
FITEM,2,72
FITEM,2,68
A,P51X
FLST,2,6,5,ORDE,2
FITEM,2,49
FITEM,2,-54
VA,P51X
FLST,2,6,5,ORDE,2
FITEM,2,43
FITEM,2,-48
VA,P51X
FLST,2,9,6,ORDE,2
FITEM,2,1
FITEM,2,-9
VOVLAP,P51X
FLST,5,6,6,ORDE,5
FITEM,5,10
FITEM,5,-11
FITEM,5,17
FITEM,5,19
FITEM,5,-21
CM,_Y,VOLU
VSEL, , , ,P51X
CM,_Y1,VOLU
CMSEL,S,_Y
CMSEL,S,_Y1
VATT, 3, , 1, 0
CMSEL,S,_Y
CMDELE,_Y
CMDELE,_Y1
CM,_Y,VOLU
VSEL, , , , 24
CM,_Y1,VOLU
CMSEL,S,_Y
CMSEL,S,_Y1
VATT, 2, , 1, 0
CMSEL,S,_Y
CMDELE,_Y
CMDELE,_Y1
SMRT,6
SMRT,1
MSHAPE,1,3D
MSHKEY,0
FLST,5,17,6,ORDE,2
FITEM,5,8
FITEM,5,-24
CM,_Y,VOLU
VSEL, , , ,P51X
CM,_Y1,VOLU
CHKMSH,'VOLU'
CMSEL,S,_Y
VMESH,_Y1
CMDELE,_Y
CMDELE,_Y1
CMDELE,_Y2
WPCSYS,-1,0
CSYS,0
WPAVE,0,0,0
CSYS,0
wpoff,0.025,0.025,0.025
```

```
wpoff,0.00375,0.006,0.02175
/UI,MESH,OFF
RACE, 0.008125, 0.010125, 0.001, 440,
0.00625, 0.026, , , 'coil1'
wpoff, 0.03,0,0
RACE, 0.008125, 0.010125, 0.001, 440,
0.00625, 0.026, , , 'coil2'
FLST,2,1,1,ORDE,1
FITEM,2,774
D,P51X,MAG,0,
FINISH
/SOL
MAGSOLV,2, , ,0.001,25,0
FINISH
```

Appendix B

CAD Drawings

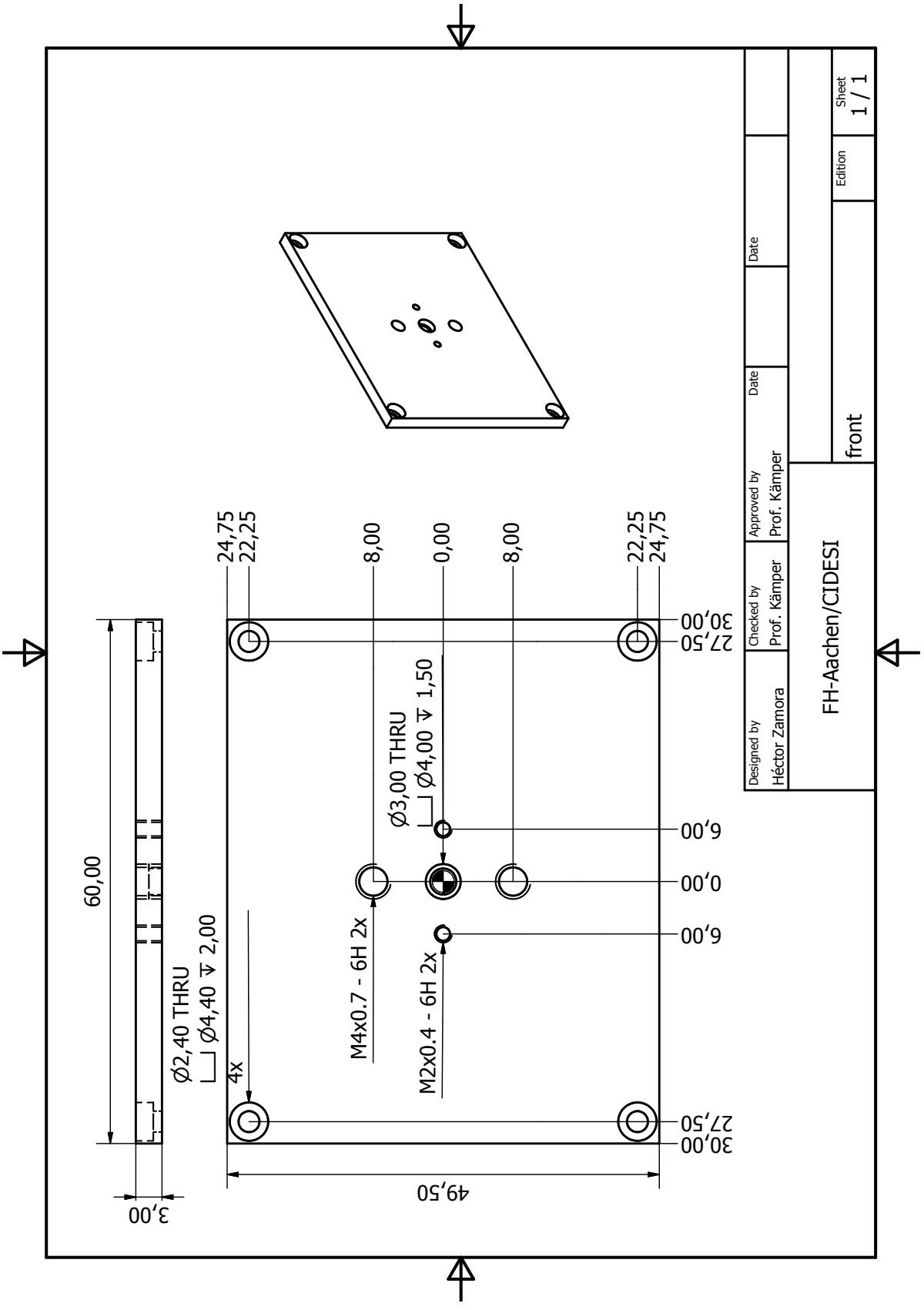

Figure B.1: Front aluminium part of the MSM actuator

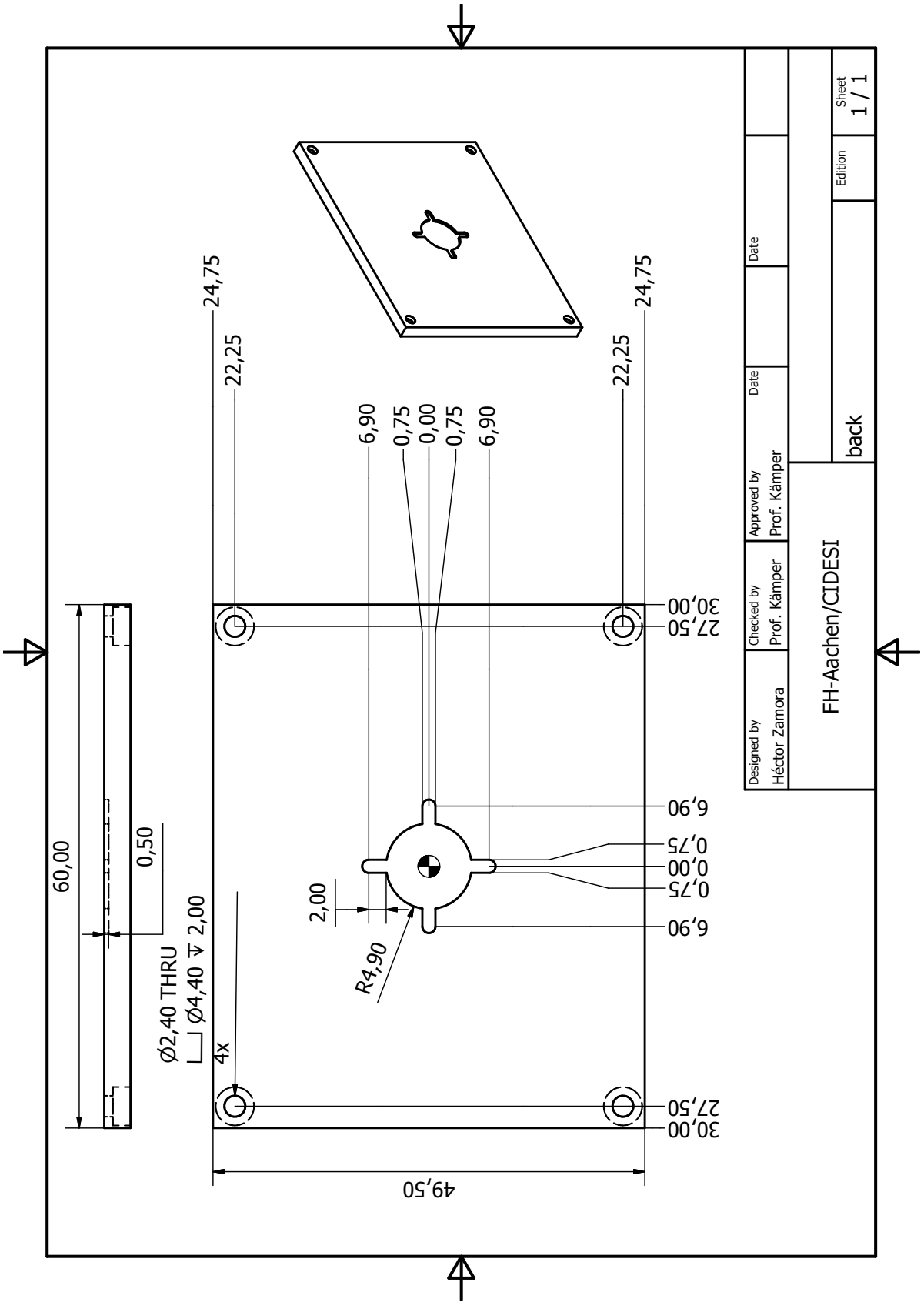

Figure B.2: Aluminium back part of the MSM actuator

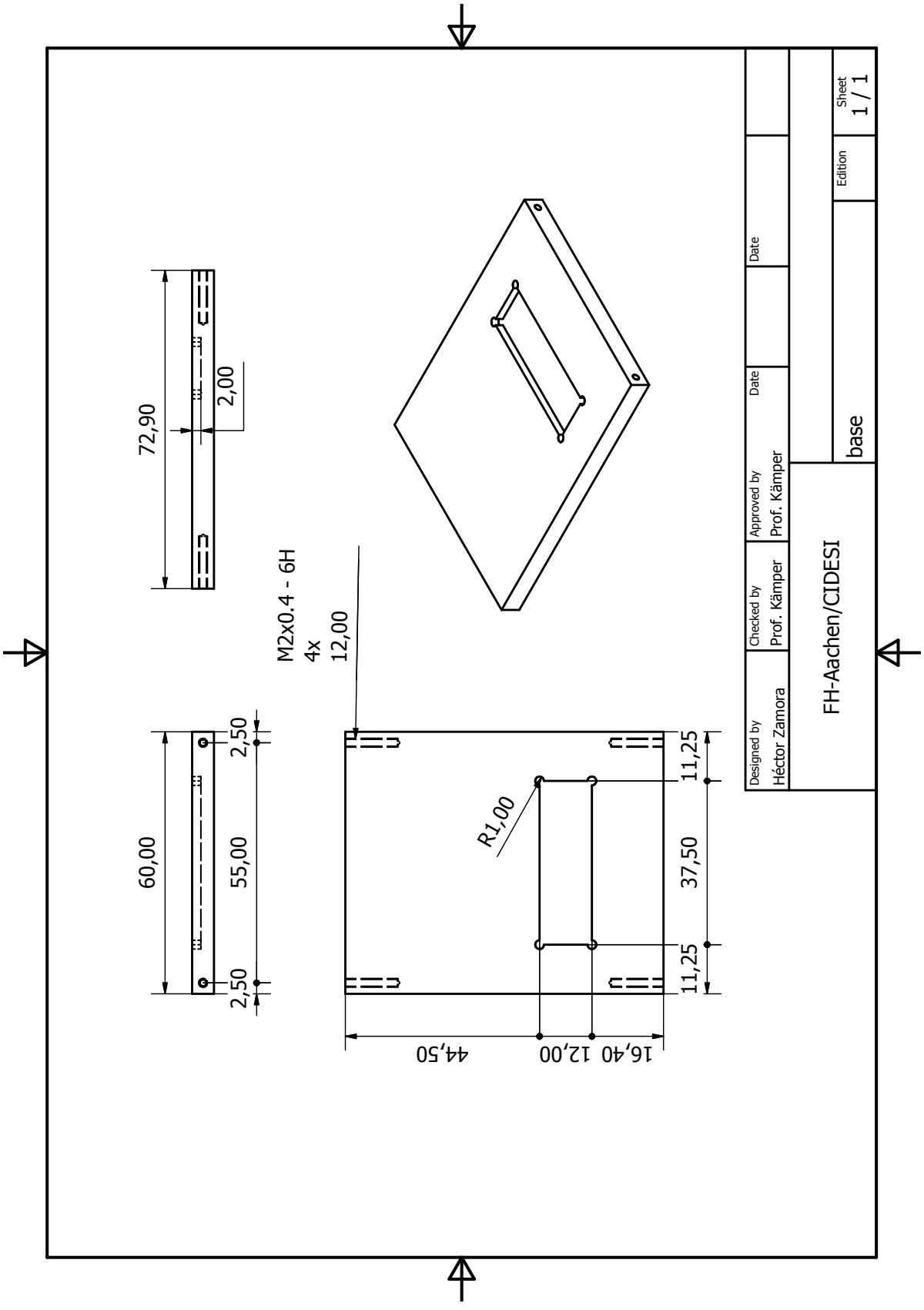

Figure B.3: Aluminium base part of the MSM actuator

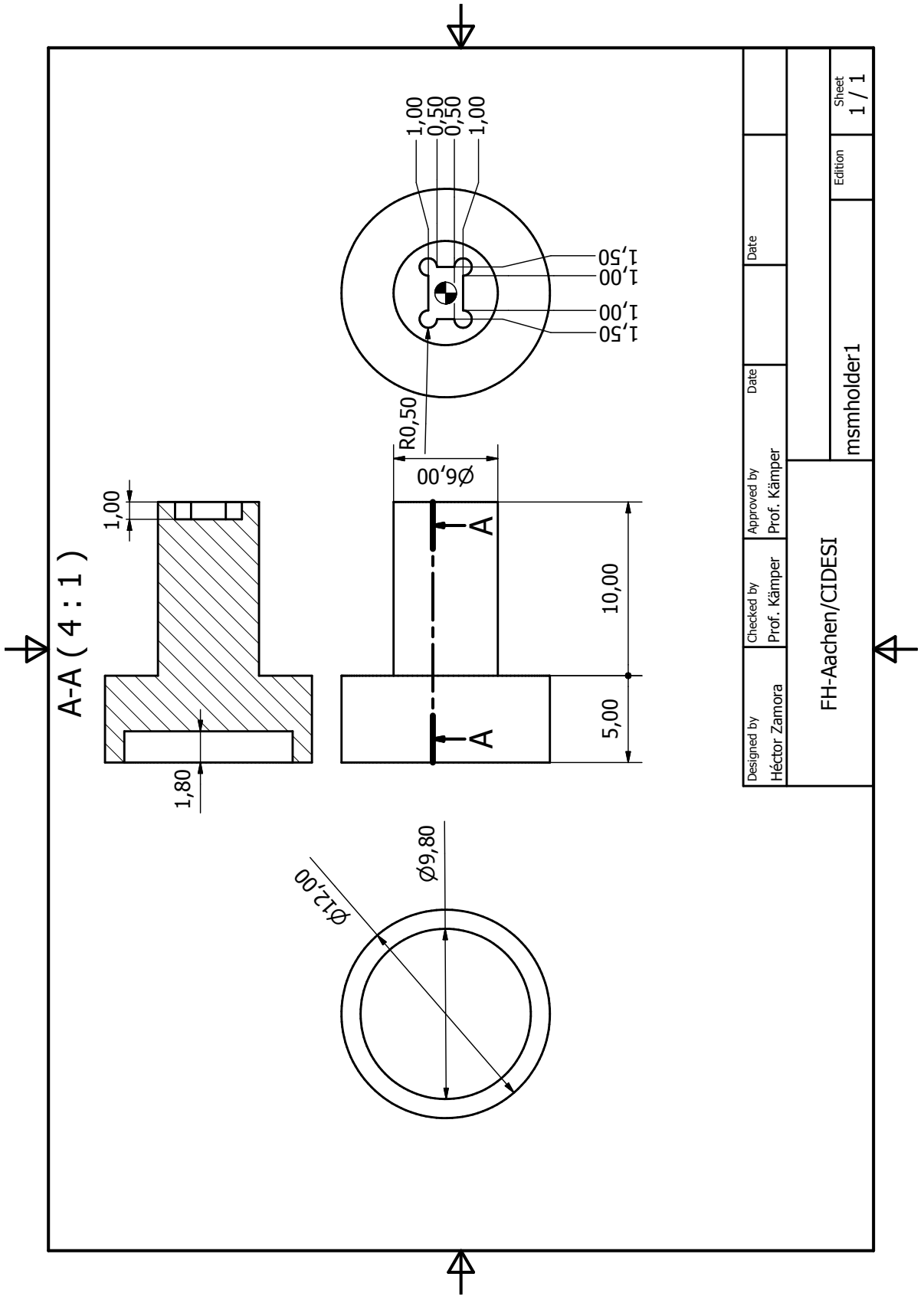

Figure B.4: Aluminium MSM holder of the MSM actuator

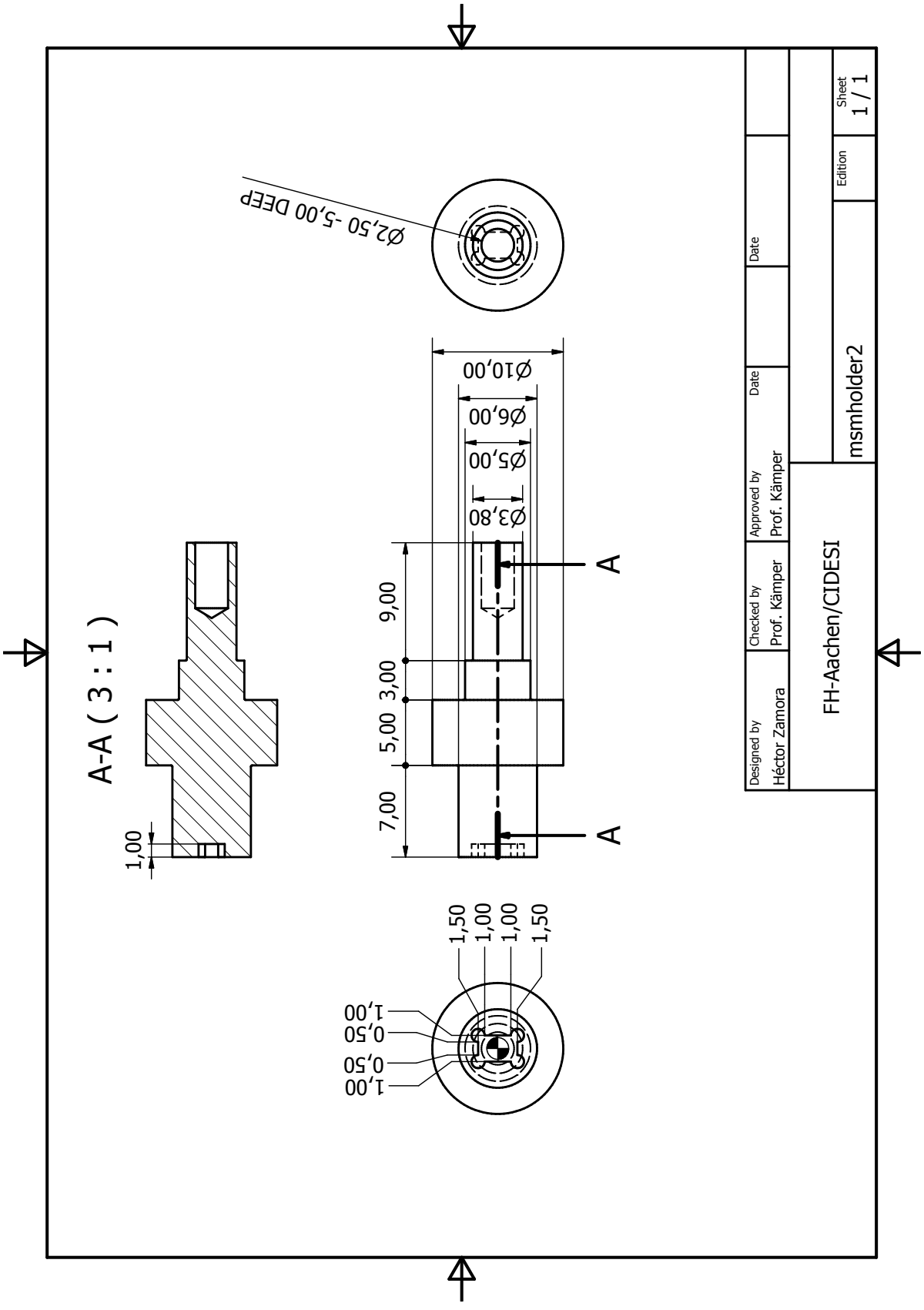

Figure B.5: Second aluminium MSM holder of the MSM actuator

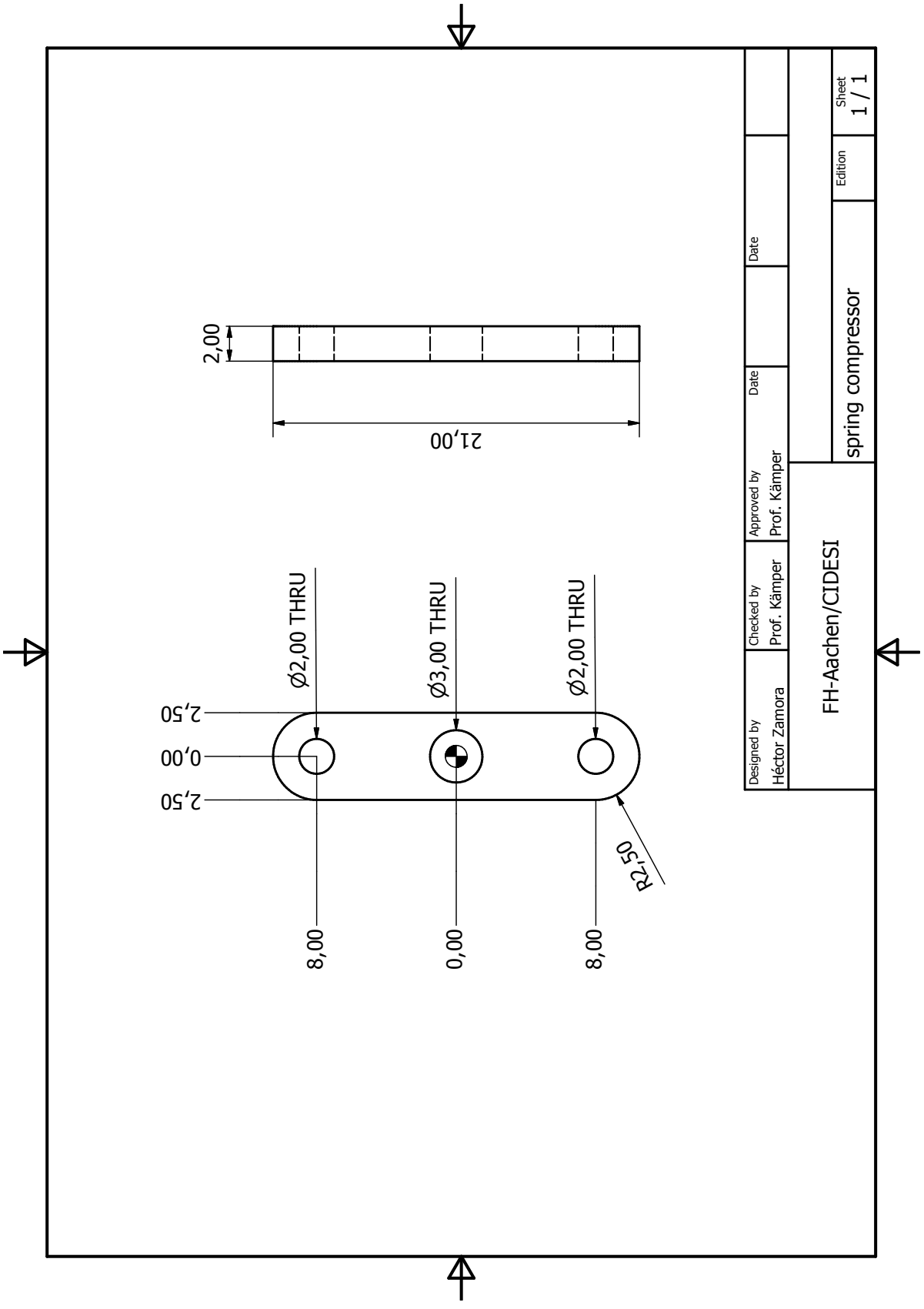

Figure B.6: Aluminium lamination to adjust the compression of the spring

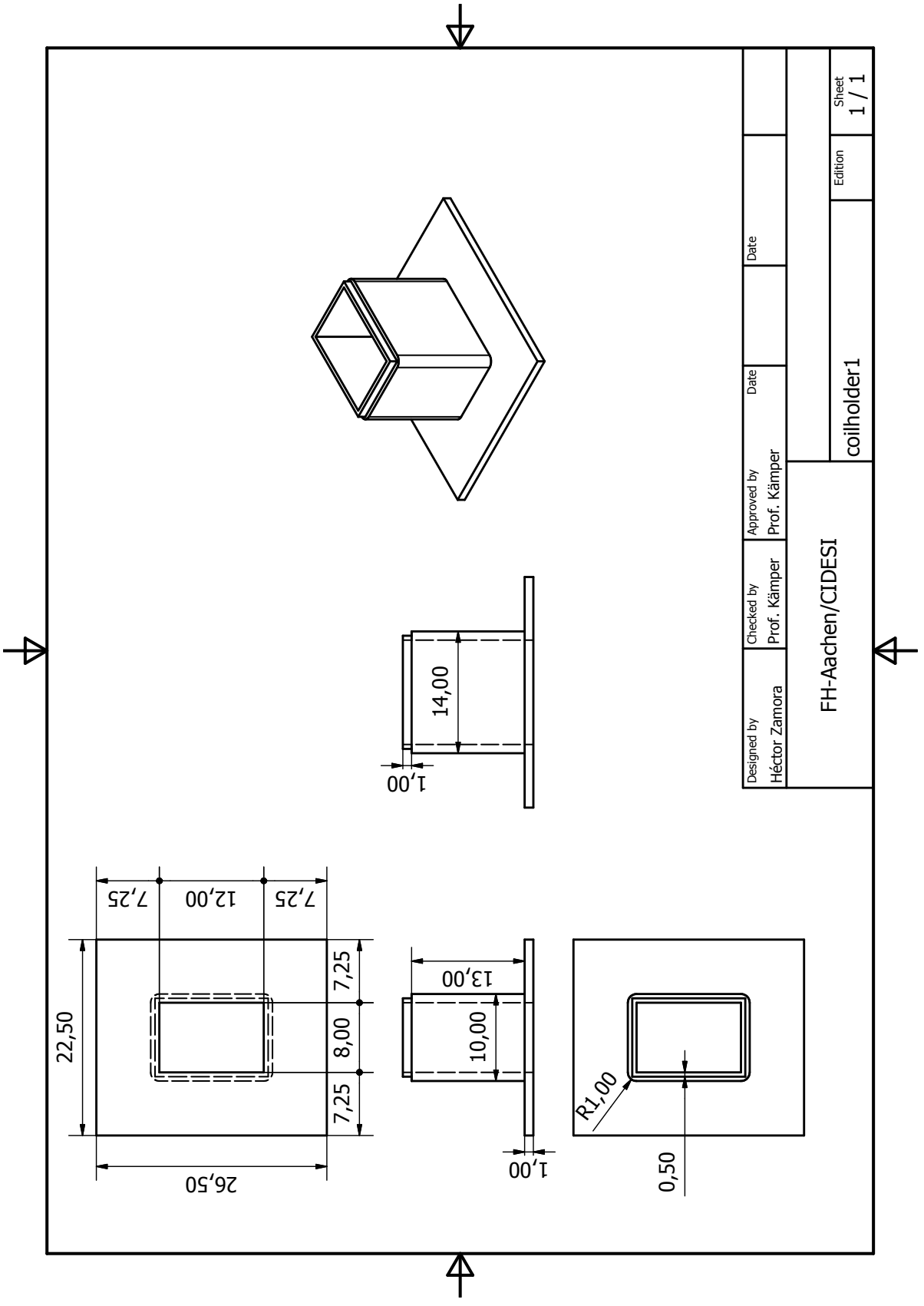

Figure B.7: Printed part to act as a support for the copper windings

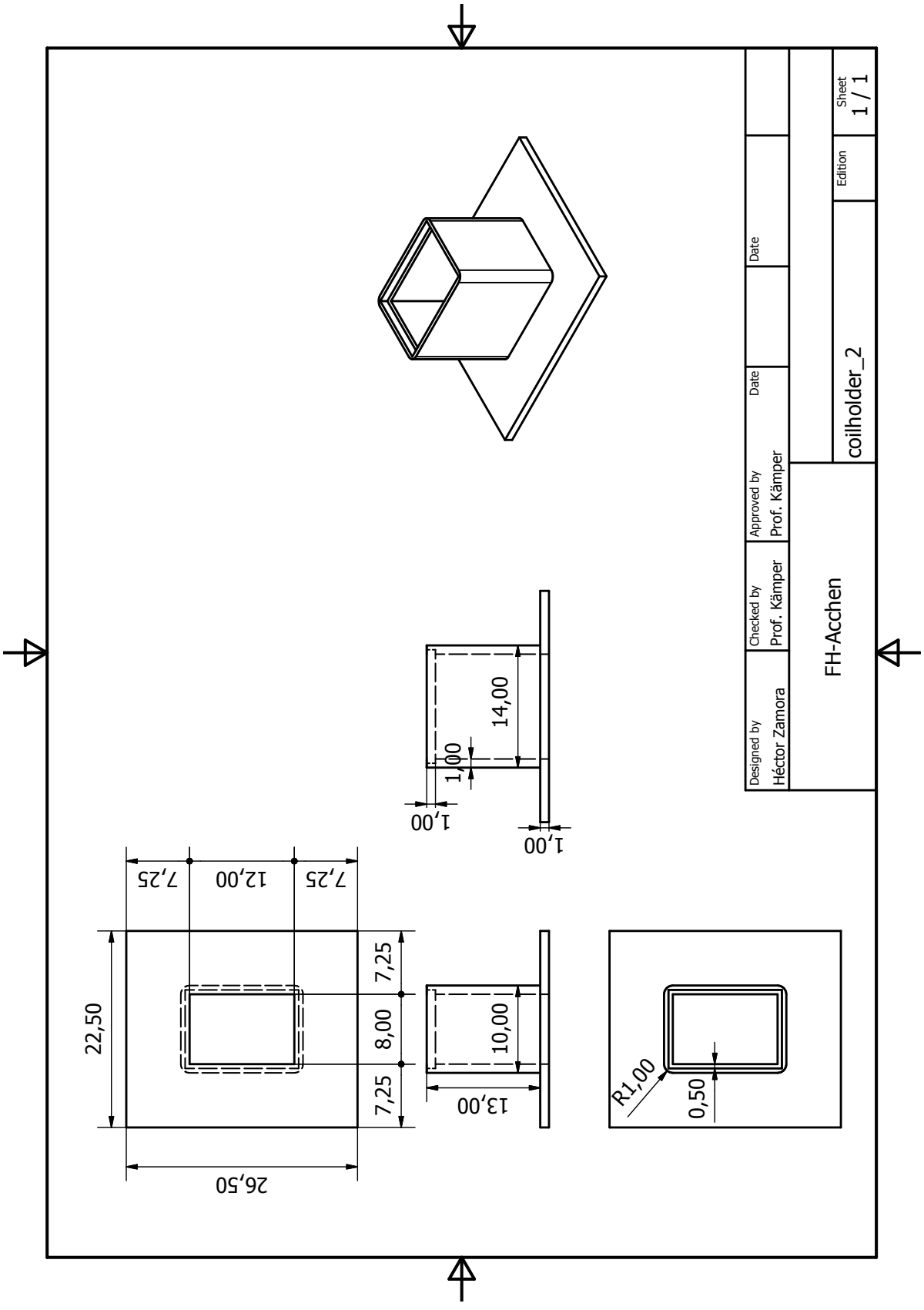

Figure B.8: Complementary printed part to act as a support for the copper windings

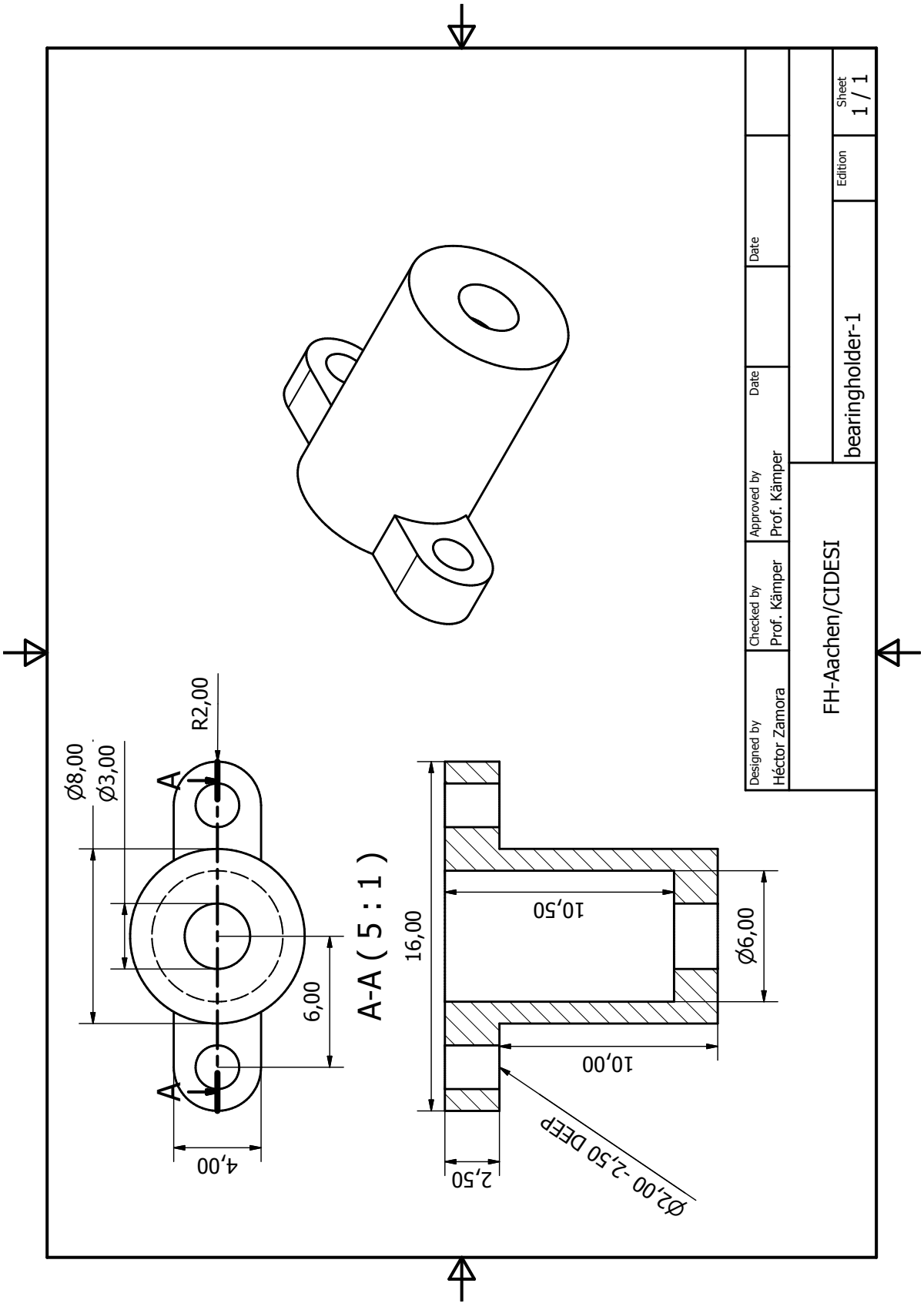

Figure B.9: Printed part to hold in place the bearing bushing

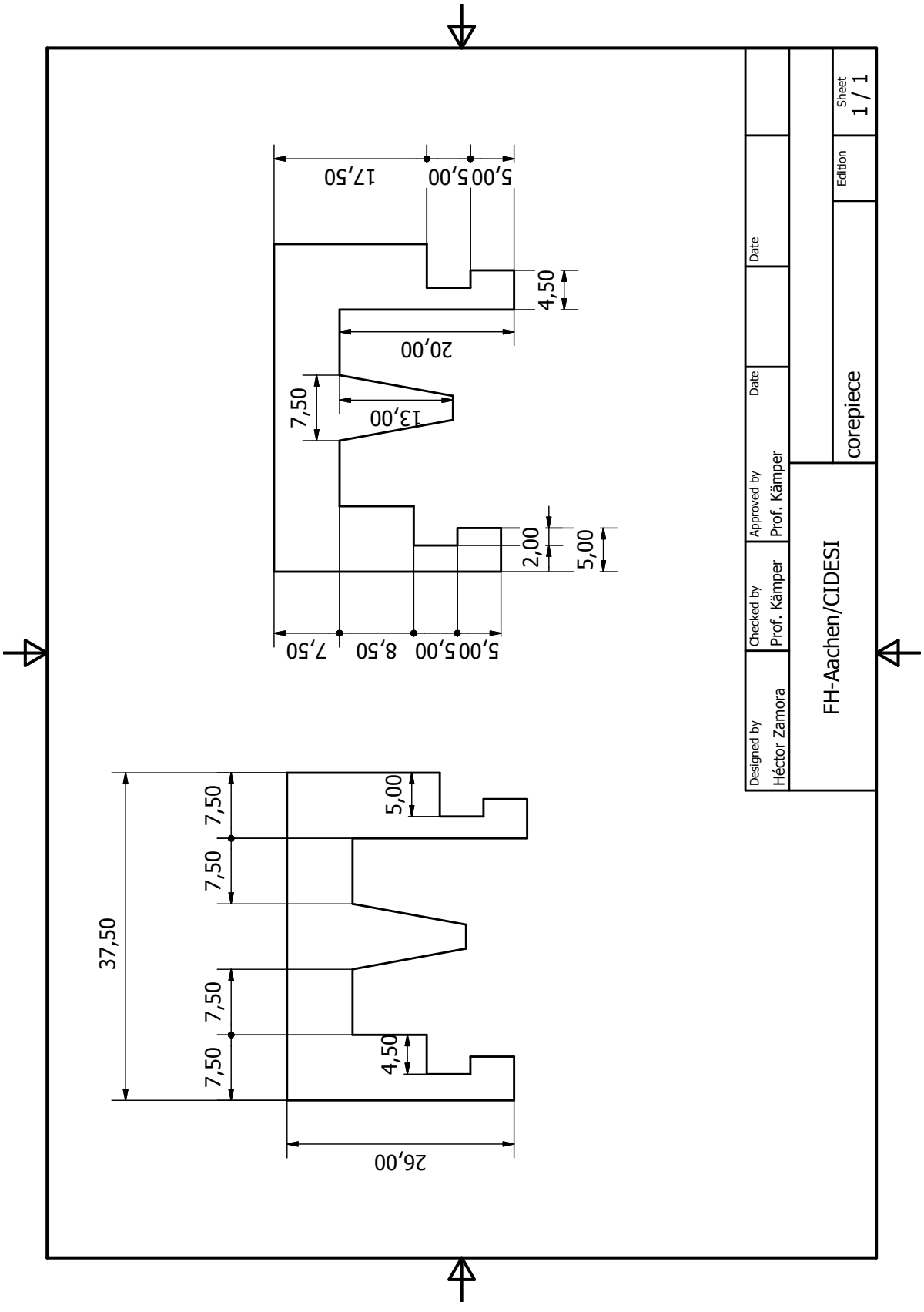

Figure B.10: Lamination of the core, designed with an interlocking leg

Appendix C

Spreadsheet with calculations of magnetic core

permeability vacuum	Diameter naked wire	Diameter varnished wire	Area of conductor	Area of square conductor	No. Turns per mm^2	Max ampacity	No. Turns
1.25664E-06	mm	mm	mm^2	mm^2	turns/mm^2	A	turns
AWG 18	1.024	1.1264	0.996495094	1.26877696	0.788160592	2.3	100
	1.024	1.1264	0.996495094	1.26877696	0.788160592	2.3	150
	1.024	1.1264	0.996495094	1.26877696	0.788160592	2.3	200
	1.024	1.1264	0.996495094	1.26877696	0.788160592	2.3	250
	1.024	1.1264	0.996495094	1.26877696	0.788160592	2.3	300
AWG 18	1.024	1.1264	0.996495094	1.26877696	0.788160592	2	100
	1.024	1.1264	0.996495094	1.26877696	0.788160592	2	150
	1.024	1.1264	0.996495094	1.26877696	0.788160592	2	200
	1.024	1.1264	0.996495094	1.26877696	0.788160592	2	250
	1.024	1.1264	0.996495094	1.26877696	0.788160592	2	300
AWG 18	1.024	1.1264	0.996495094	1.26877696	0.788160592	2.5	100
	1.024	1.1264	0.996495094	1.26877696	0.788160592	2.5	150
	1.024	1.1264	0.996495094	1.26877696	0.788160592	2.5	200
	1.024	1.1264	0.996495094	1.26877696	0.788160592	2.5	220
	1.024	1.1264	0.996495094	1.26877696	0.788160592	2.5	250
	1.024	1.1264	0.996495094	1.26877696	0.788160592	2.5	300
AWG 20	0.8128	0.89408	0.627830835	0.799379046	1.250970994	2	100
	0.8128	0.89408	0.627830835	0.799379046	1.250970994	2	150
	0.8128	0.89408	0.627830835	0.799379046	1.250970994	2	200
	0.8128	0.89408	0.627830835	0.799379046	1.250970994	2	220
	0.8128	0.89408	0.627830835	0.799379046	1.250970994	2	250
	0.8128	0.89408	0.627830835	0.799379046	1.250970994	2	300
AWG 22	0.64516	0.709676	0.395557951	0.503640025	1.985545132	1	100
	0.64516	0.709676	0.395557951	0.503640025	1.985545132	1	150
	0.64516	0.709676	0.395557951	0.503640025	1.985545132	1	200
	0.64516	0.709676	0.395557951	0.503640025	1.985545132	1	250
	0.64516	0.709676	0.395557951	0.503640025	1.985545132	1	300
	0.64516	0.709676	0.395557951	0.503640025	1.985545132	1	400

Figure C.1: Spreadsheet with data of different values for the calculation of the magnetic core

Flux density needed		Area of coil winding	Length window	Length gap	Length magnetic circuit Eshape 3 gaps	Length magnetic E shape 1 gap	Length magnetic C shape
T		mm^2	mm	mm	m	m	m
	1	126.877696	11.264	0.5	-0.307315651	-0.140648984	0.078053048
	1	190.316544	13.79552623	0.5	-0.210973476	-0.044306809	0.367079572
	1	253.755392	15.92970157	0.5	-0.114631301	0.052035366	0.656106097
	1	317.19424	17.80994778	0.5	-0.018289126	0.14837754	0.945132621
	1	380.633088	19.5098203	0.5	0.078053048	0.244719715	1.234159145
	1	126.877696	11.264	0.5	-0.332448392	-0.165781725	0.002654825
	1	190.316544	13.79552623	0.5	-0.248672588	-0.082005921	0.253982237
	1	253.755392	15.92970157	0.5	-0.164896784	0.001769883	0.505309649
	1	317.19424	17.80994778	0.5	-0.08112098	0.085545687	0.756637061
	1	380.633088	19.5098203	0.5	0.002654825	0.169321491	1.007964474
	1	126.877696	11.264	0.5	-0.29056049	-0.123893823	0.128318531
	1	190.316544	13.79552623	0.5	-0.185840735	-0.019174068	0.442477796
	1	253.755392	15.92970157	0.5	-0.08112098	0.085545687	0.756637061
	1	279.1309312	16.70721195	0.5	-0.039233077	0.127433589	0.882300768
	1	317.19424	17.80994778	0.5	0.023598776	0.190265442	1.070796327
	1	380.633088	19.5098203	0.5	0.128318531	0.294985197	1.384955592
	1	79.93790464	8.9408	0.5	-0.332448392	-0.165781725	0.002654825
	1	119.906857	10.95019895	0.5	-0.248672588	-0.082005921	0.253982237
	1	159.8758093	12.64420062	0.5	-0.164896784	0.001769883	0.505309649
	1	175.8633902	13.26134949	0.5	-0.131386462	0.035280205	0.605840614
	1	199.8447616	14.13664605	0.5	-0.08112098	0.085545687	0.756637061
	1	239.8137139	15.48591986	0.5	0.002654825	0.169321491	1.007964474
	1	50.3640025	7.09676	0.5	-0.416224196	-0.249557529	-0.248672588
	1	75.54600375	8.691720413	0.5	-0.374336294	-0.207669627	-0.123008882
	1	100.728005	10.03633424	0.5	-0.332448392	-0.165781725	0.002654825
	1	125.9100062	11.2209628	0.5	-0.29056049	-0.123893823	0.128318531
	1	151.0920075	12.29194889	0.5	-0.248672588	-0.082005921	0.253982237
	1	201.45601	14.19352	0.5	-0.164896784	0.001769883	0.505309649

$$l'_m = \left(\frac{2Ni}{3B} - \frac{l_g}{\mu_o}\right)\mu_r\mu_o \qquad l'_m = \left(\frac{2Ni}{3B} - \frac{2l_g}{3\mu_o}\right)\mu_r\mu_o \qquad l'_m = \left(\frac{2Ni\mu_r\mu_o}{B} - l_g\mu_r\right)$$

Figure C.2: Spreadsheet with data of different values for the calculation of the magnetic core (cont.)

Appendix D

LabVIEW code

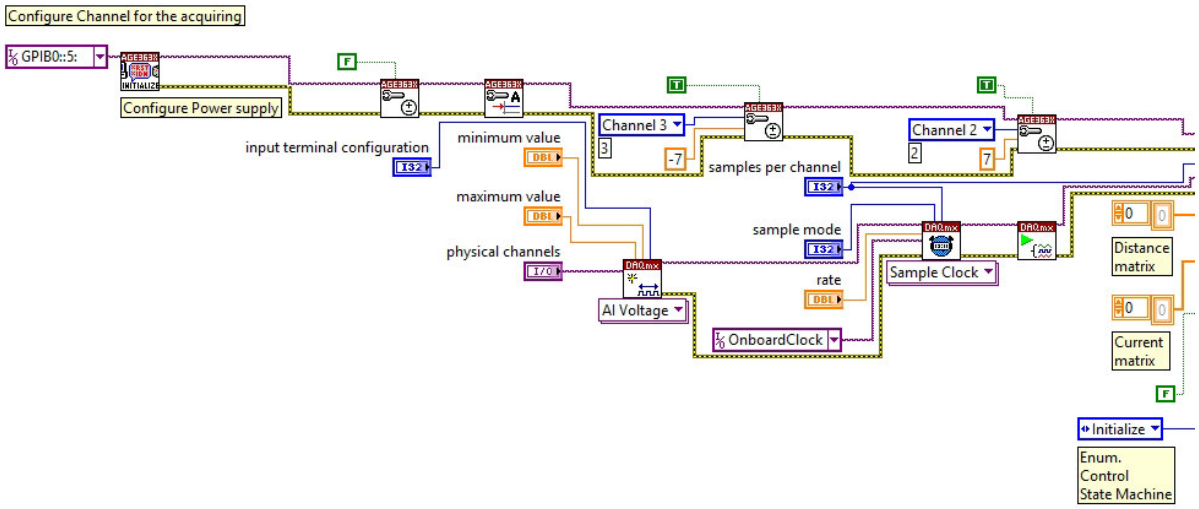

Figure D.1: LabVIEW code for configuring the channels and power supplies.

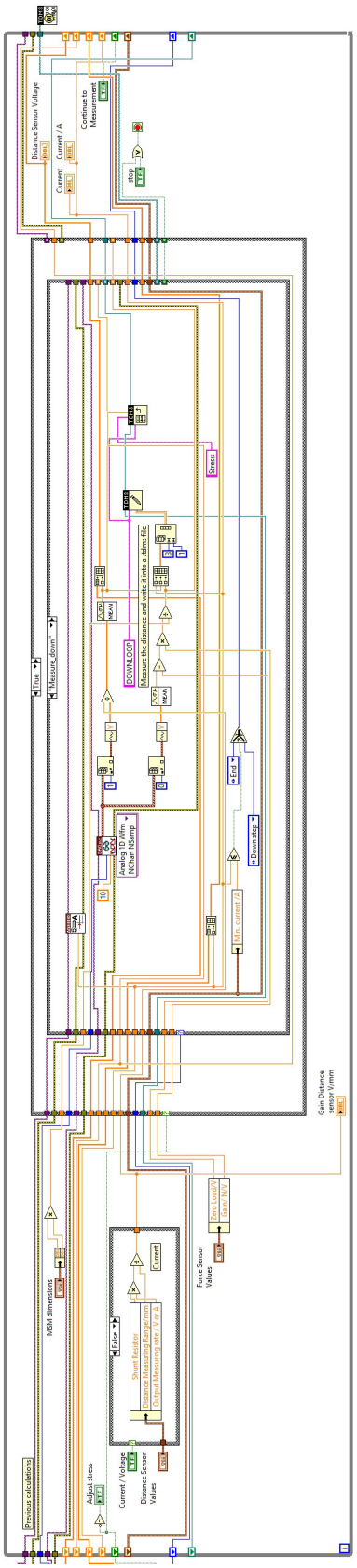

Figure D.2: Main LabVIEW case

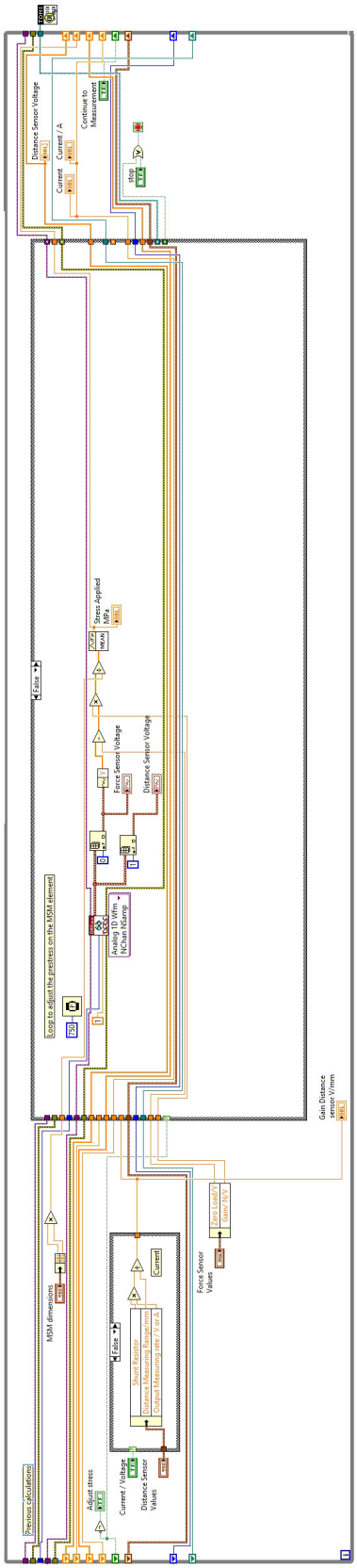

Figure D.3: Main LabVIEW case (cont.)

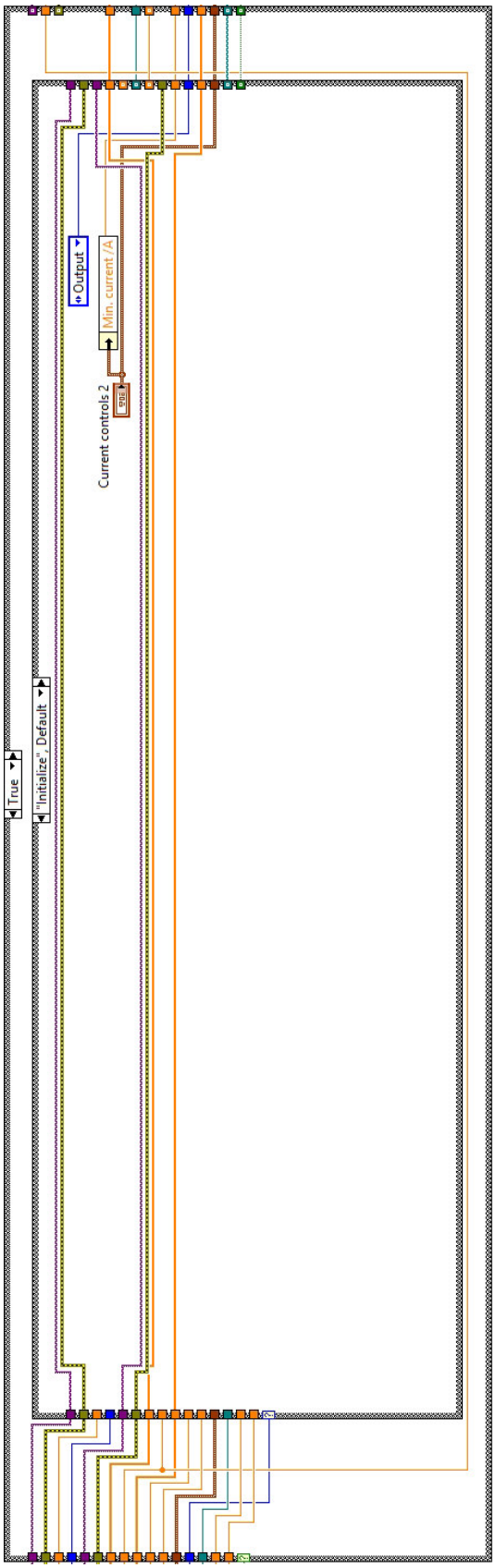

Figure D.4: First step of the state machine. Sets the minimum current applied to the MSM

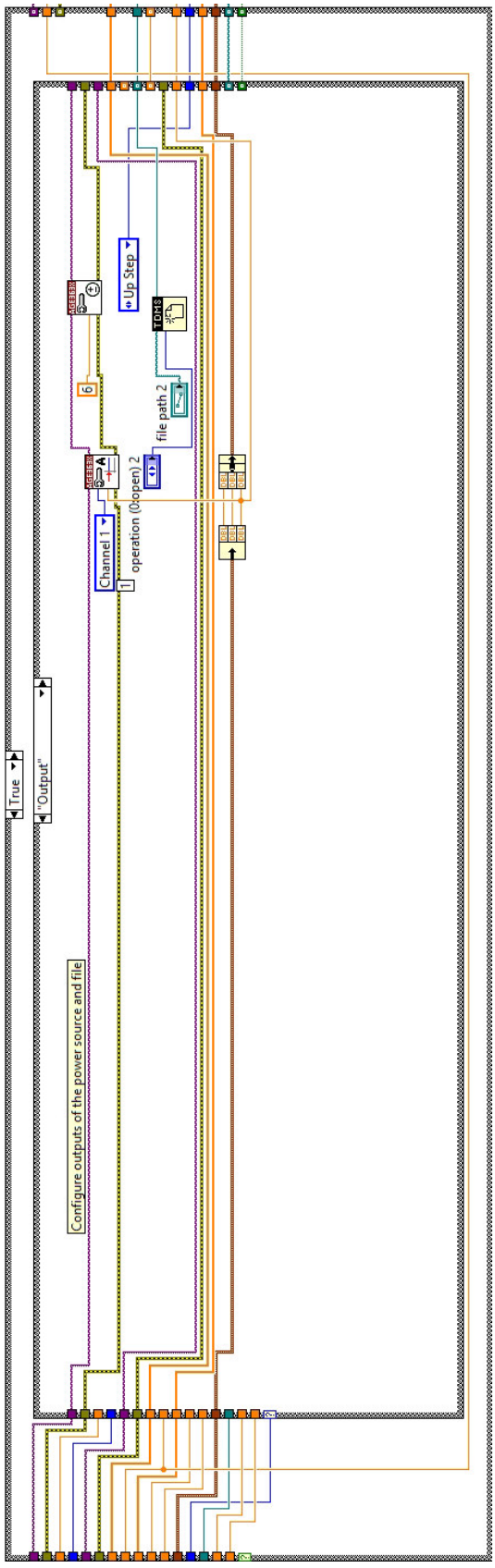

Figure D.5: Step to set the output values on the current supply sources

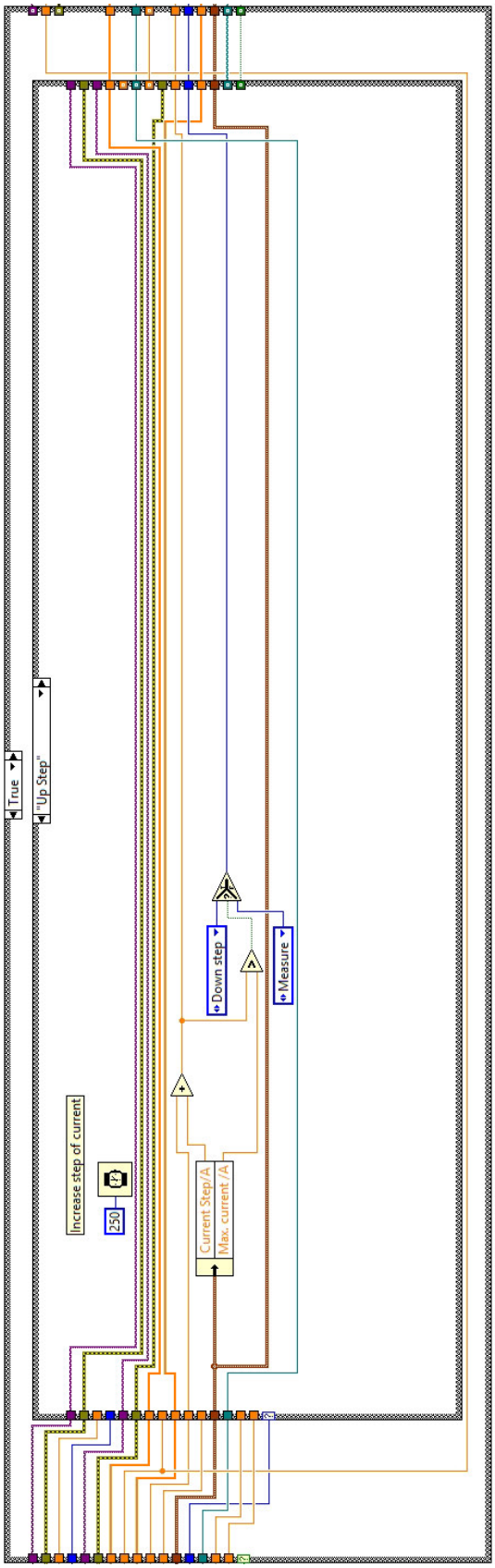

Figure D.6: Step of the state machine which increases the applied current by a step

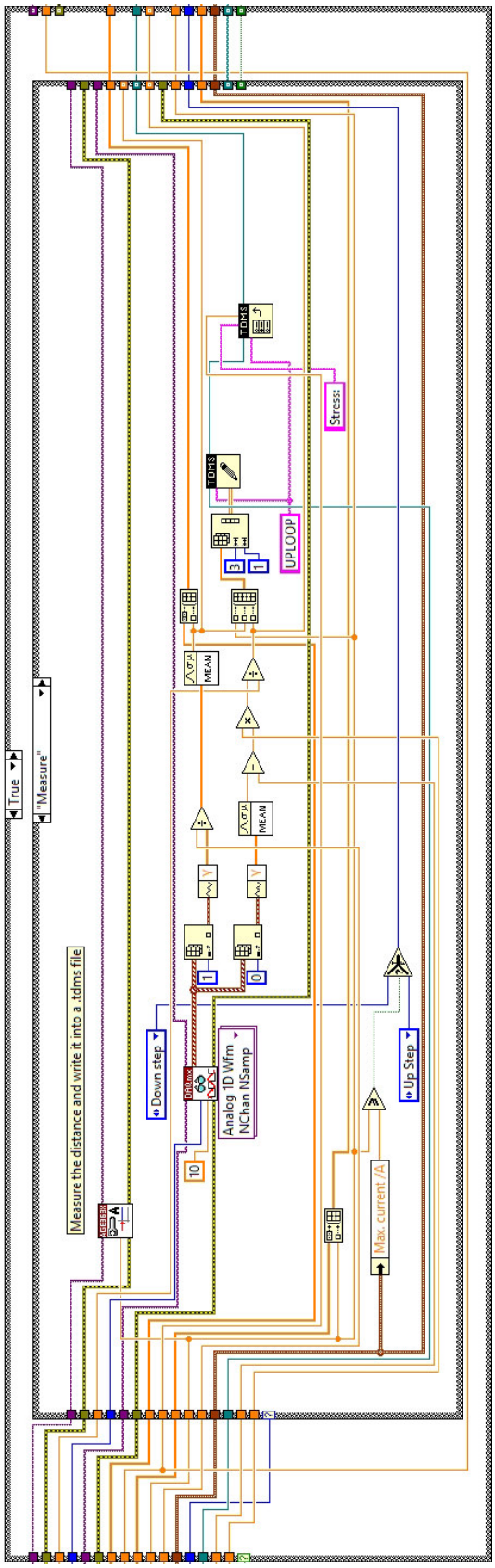

Figure D.7: Measuring step of the state machine, the data is saved on a .tdms file

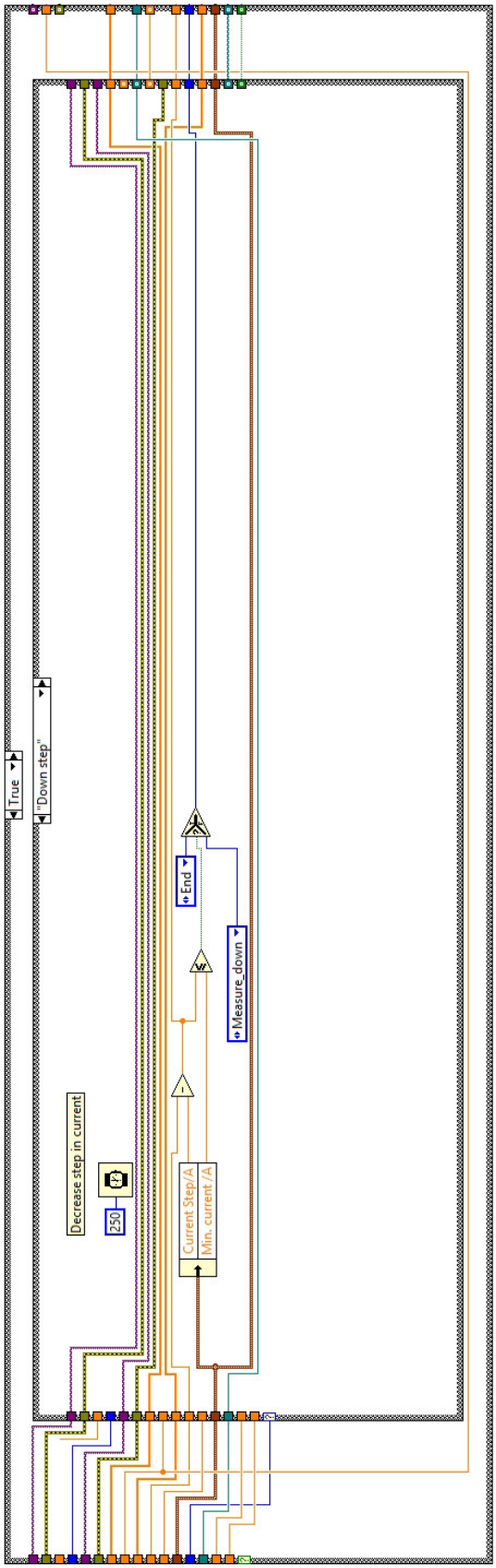

Figure D.8: State which decreases the value of the current applied

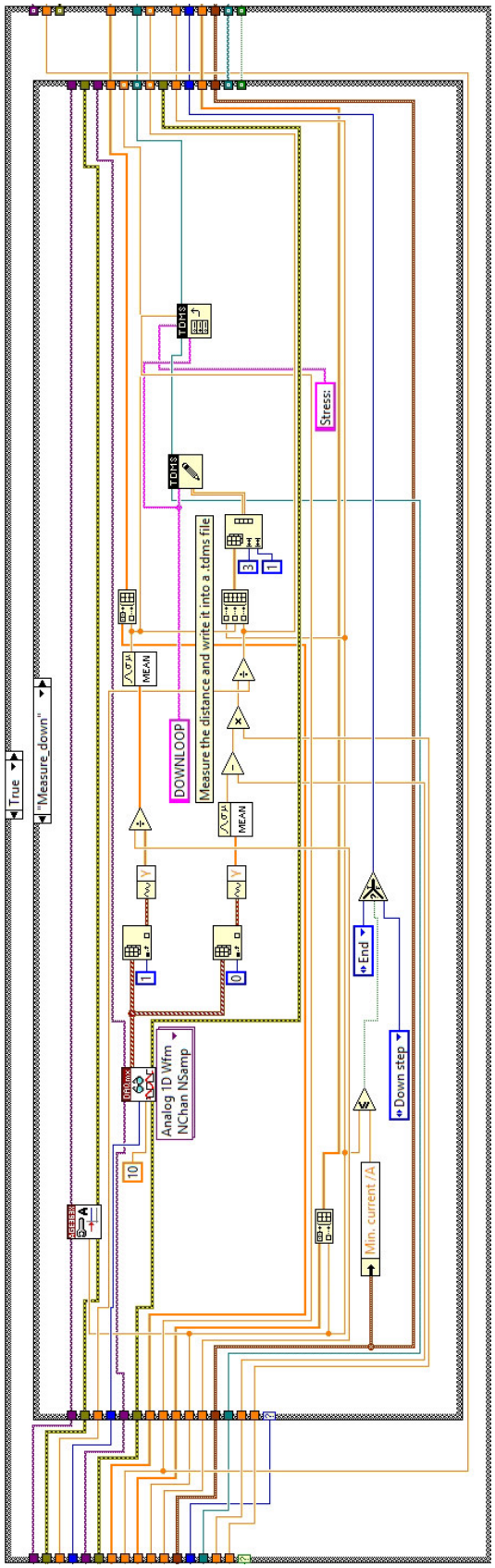

Figure D.9: Measuring state for the down loop, the values are saved in a different group of the .tdms file

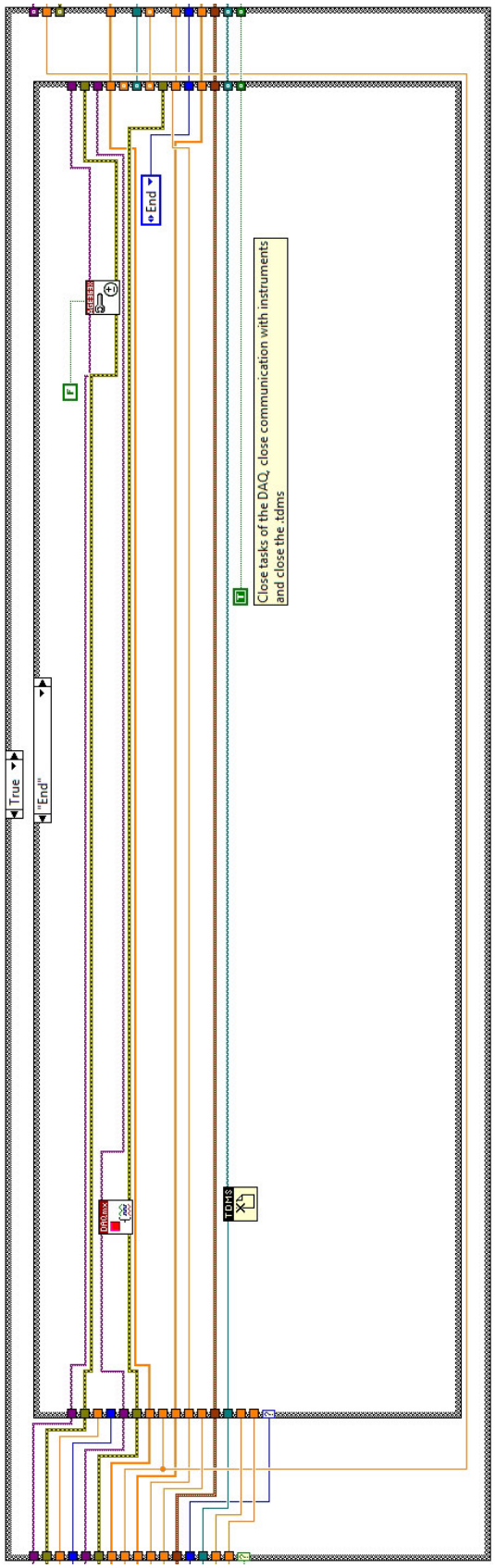

Figure D.10: Step which closes the .tdms file, shuts down the power supplies and stops the tasks and the DAQ